A&A, 711, A125 (2026)
https://doi.org/10.1051/0004-6361/202659855
© The Authors 2026

Astronomy & Astrophysics

MINDS survey of silicates in T Tauri disks: Correlation between dust and gas

J. Varga[1,⋆], Th. Henning[2], L. B. F. M. Waters[3,4], I. Kamp[5], Á. Kóspál[1,6,2], P. Ábrahám[1,6,7], O. Absil[8], A. M. Arabhavi[5], D. Gasman[9], S. L. Grant[10,11], M. Güdel[7,12,13], H. Jang[3], T. Kaeufer[14], J. Kanwar[15], N. T. Kurtovic[10], P.-O. Lagage[16], G. Perotti[17,2], A. Somigliana[2], L. M. Stapper[2], B. Tabone[18], M. Temmink[19], E. F. van Dishoeck[19,10], and M. Vlasblom[19]

(Affiliations can be found after the references)

Received 14 March 2026 / Accepted 2 June 2026

ABSTRACT

Context. Silicates are key constituents of planet-forming disks and are among the most important building blocks of rocky planets. Mid-infrared spectral features of micron-sized silicate grains are powerful tracers of grain growth, mineralogy, and disk chemistry.
Aims. We characterized the dust mineralogy in T Tauri disks using James Webb Space Telescope (JWST)/Mid-Infrared Instrument (MIRI) observations. A further aim of ours was to investigate the connections between the dust and molecular gas compositions.
Methods. We analyzed JWST/MIRI spectra of 26 disks as part of the MIRI mid-Infrared Disk Survey (MINDS). We employed spectral decomposition with our new `DustComp` tool to derive the mass fractions of individual dust species. We included in our fits Mg_2SiO_4 (forsterite), $MgSiO_3$ (enstatite), and SiO_2 (silica) together with amorphous silicates of corresponding stoichiometry.
Results. We find that Mg-rich (and Fe-poor) silicates represent our data well. Fit residuals are typically within ±3%. Grain size distributions are skewed toward larger sizes (>2 μm), indicating significant growth. Large (∼5 μm-sized) amorphous Mg-silicates were robustly detected, whereas the presence of large crystalline grains could not be firmly established. The average dust composition is dominated by grains of Mg_2SiO_4 stoichiometry (∼60%, including amorphous and crystalline state), followed by $MgSiO_3$ (∼30%) and SiO_2 (∼10%). The mass fractions of crystalline grains are typically in the 5–24% range, with a mean of 14%. We robustly detected annealed silica in nine objects, with cristobalite as the main polymorph. We found a correlation between dust and molecular gas composition: disks with strong annealed silica features show relatively strong CO_2 emission, while forsterite-rich disks display stronger H_2O emission. Disks with annealed silica features may also have elevated gas-phase C/O ratios, suggesting a process, such as dust sublimation and recondensation, that establishes thermo-chemical equilibrium between solids and gas.
Conclusions. The correlation between dust and gas may provide the first indication that the molecular gas composition regulates the availability of dust species in the inner disk.

Key words. methods: data analysis – planets and satellites: formation – protoplanetary disks – stars: pre-main sequence – stars: variables: T Tauri, Herbig Ae/Be – infrared: planetary systems

1. Introduction

Cosmic dust is produced in the outflows of asymptotic giant branch stars and supernovae (Salpeter 1977; Gail & Sedlmayr 1999; Todini & Ferrara 2001; Höfner & Olofsson 2018) and subsequently enriches the interstellar medium (ISM). There are strong indications that dust is also formed in the denser phases of the ISM (e.g., Draine 2003; Zhukovska et al. 2018). The ISM dust is rich in Mg-silicates, in the form of submicron-sized amorphous grains with olivine and pyroxene stoichiometry (Kemper et al. 2004; Min et al. 2007; Henning 2010). These silicate grains can be readily detected due to their spectral resonances in the mid-infrared (mid-IR), which are seen as absorption (Kemper et al. 2004) or emission features (Tielens et al. 1998). Silicates are not the only type of solids in astrophysical environments, though. There is direct and indirect evidence of other cosmic dust materials, including iron, various oxides, carbides, sulfides, carbonates, ices, and various forms of carbon (Dorschner & Henning 1995; Henning & Salama 1998; Henning & Meeus 2011; Tielens 2022).

During star formation, ISM dust is incorporated into the planet-forming disks encircling young stars. In these disks, as a first step of planet formation, dust grains start to grow by sticking together (Brauer et al. 2008; Testi et al. 2014; Birnstiel 2024). Moreover, in high temperature disk regions ($T \gtrsim 1000$ K), grains can be annealed, change their chemical composition, or even sublimate (e.g., Fabian et al. 2000; D'Alessio et al. 2005; Houge et al. 2025). Dust can also form in situ in disks by condensation from the gas phase. In the hot inner regions, the sublimation of dust followed by recondensation can lead to chemical reprocessing of the original material. This process has been extensively studied in the context of equilibrium condensation, which predicts the sequence of mineral formation as a function of temperature and pressure (e.g., Lodders & Fegley 2002; Lodders 2003; Ebel 2006). The studies established a condensation sequence in which corundum (Al_2O_3), Ca-Al-oxides, and various Ca–Ti-minerals condense first (at $T \sim 1500$–1700 K) from a cooling gas of solar composition gas. At lower temperatures ($T \sim 1300$–1400 K) iron and Mg-silicates condense, followed by troilite (FeS) at $T \sim 700$ K.

Laboratory measurements of cosmic silicate analogs have shown that the positions and shapes of the mid-IR dust spectral features are influenced by the size, shape, lattice structure, and temperature of the grains, in addition to their chemical composition (Henning & Stognienko 1993; Jäger et al. 1994;

⋆ Corresponding author: `varga.jozsef@csfk.org`

Open Access article, published by EDP Sciences, under the terms of the Creative Commons Attribution License (https://creativecommons.org/licenses/by/4.0), which permits unrestricted use, distribution, and reproduction in any medium, provided the original work is properly cited.
This article is published in open access under the Subscribe to Open model. Subscribe to A&A to support open access publication.

Fabian et al. 2001; Min et al. 2005, 2007; Zeidler et al. 2015). For example, crystalline grains can be identified by their sharp spectral features, such as the peaks at 10.0, 11.3, 16.3, 19.5, and 23.5 μm from forsterite and the 9.3, 10.4, and 19.4 μm peaks from enstatite (Jäger et al. 1998). By comparing these laboratory data to observed disk spectra, it became possible to infer the physical and chemical properties of the grains emitting those features.

Observations showed that there is a large variety in the spectral feature shapes of planet-forming disks, suggesting that their dust underwent processing (e.g., Waelkens et al. 1996; Malfait et al. 1998; van Boekel et al. 2005; Furlan et al. 2011). Indeed, sample studies provided ample evidence of grain growth and crystallization in disks (Bouwman et al. 2001; van Boekel et al. 2003; Przygodda et al. 2003; Bouwman et al. 2008; Watson et al. 2009). The mass fraction in crystalline silicates (relative to the total silicate mass) was found to be typically ∼10%, although there is a large diversity among the individual sources (between ∼1% to ∼30% Honda et al. 2006; Bouwman et al. 2008; Meeus et al. 2009; Juhász et al. 2010; Olofsson et al. 2010). For detailed reviews on cosmic silicates and dust processing, we refer to Henning (2010) and Henning & Meeus (2011).

To date, the c2d survey with Spitzer/IRS has provided the most comprehensive spectroscopic study of silicates in T Tauri disks (Kessler-Silacci et al. 2006). The survey provided several important results. The shapes of the silicate spectral features indicate fast grain growth from 0.1 μm to ∼1 μm in radius. The ∼10 μm feature strength versus feature shape trend is not correlated with the ages of the systems, indicating that mixing and regeneration of small grains are occurring. Olofsson et al. (2009) found that the silicates in their sample of T Tauri and Herbig Ae/Be disks are Mg-rich and Fe-poor, and the majority of the objects show at least some emission from crystalline grains. They noted that the 10 μm and $\lambda > 20$ μm spectral features originate from different disk zones: the shorter wavelength is from a warm zone at $r \sim 1$ au, and the longer wavelengths are from a colder zone extending to $r \sim 10$ au. They also discovered a crystallinity paradox: Crystalline silicate features occur at longer wavelengths ($\lambda > 20$ μm) more frequently than at 10 μm, suggesting a significant reservoir of cold crystals in the outer disk zones. This is contrary to the expectations, which predict an increased crystallinity fraction in the innermost disk zones due to thermal annealing at $T \gtrsim 1000$ K (Hallenbeck et al. 1998; Fabian et al. 2000).

Olofsson et al. (2010) subsequently suggested that the presence of cold crystals can be attributed to efficient radial mixing, which distributes crystalline grains at large distances from the central star. Alternatively, shock waves either by gravitational instability or by embedded planets may also be able to anneal the grains in the outer disk (Harker & Desch 2002). The 2008 outburst of the young eruptive star EX Lup provided backing to the radial mixing scenario. Ábrahám et al. (2009) detected newly formed crystalline silicates in the disk after the outburst of EX Lup. Following a careful analysis of dust spectral features prior, during, and after the outburst, Juhász et al. (2012) concluded that the crystals that formed in the inner disk within ∼1 au had been transported to larger radii, giving rise to the longer ($\lambda > 20$ μm) wavelength crystalline silicate features a year after the outburst.

It has turned out to be difficult to find firm relations between the mineralogy and other system parameters (e.g., age, spectral type, disk mass) in planet-forming disks (e.g., Honda et al. 2006; Watson et al. 2009; Oliveira et al. 2011). Kessler-Silacci et al. (2006) and later Furlan et al. (2011) found that the 10 μm silicate feature tends to be weaker and flatter for disks around very low mass stars (VLMSs, spectral types M6–M9), and Furlan et al. (2011) attributed these characteristics to the presence of generally more processed dust in those objects. Glauser et al. (2009) found that high-energy particles are relevant for amorphizing crystals in young disks based on both observations of T Tauri stars and simulations.

For a sample of Herbig Ae/Be disks observed with Spitzer/IRS, Juhász et al. (2010) found that their dust mainly consists of amorphous silicates with olivine and pyroxene stoichiometry, crystalline forsterite, crystalline enstatite, and silica. This is in line with the results of the c2d survey for T Tauri disks. They also showed that enstatite is more concentrated toward the warm inner regions, compared to forsterite, which is in contrast to predictions of equilibrium condensation models. This result is in agreement with the findings of Bouwman et al. (2008), who compared the relative abundances of forsterite and enstatite in the warm inner versus cold outer disk zones for a sample of seven planet-forming disks, mostly T Tauris. They found that more enstatite than forsterite occurs in the inner warm zone (at ∼1 au), while forsterite dominates the cold outer zone. They argued that this pattern is more consistent with a localized crystallization scenario rather than with radial mixing. To sum up these Spitzer/IRS results, pathways of dust processing are highly diverse in planet-forming disks: Crystals may form locally in the outer disk zones, but radial mixing can also occur, transporting crystals from the warm inner regions to the cold outer disk.

While Spitzer/IRS spectra provide indirect spatial information, IR interferometric instruments such as VLTI/MIDI and VLTI/MATISSE can directly probe the radial distribution of dust in disks. These VLTI observations confirmed an increased crystallinity fraction in the innermost disk regions ($r \lesssim 1$ au), in agreement with the thermal annealing scenario (van Boekel et al. 2004, 2006; Varga et al. 2018, 2024). The spatial distribution of cold crystals emitting at $\lambda > 20$ μm could not be studied with these instruments, as they do not cover that wavelength range.

Silica (SiO_2) is a minor constituent of dust in planet-forming disks, occurring mostly in amorphous form, but Sargent et al. (2009a) also detected crystalline SiO_2 in five T Tauri disks. They suggested that the formation of annealed silica requires high temperatures (1200–1300 K, Fabian et al. 2000) followed by rapid cooling, implying transient heating events similar to those hypothesized to have created Solar System chondrules.

Compared to Spitzer/IRS, the Mid Infrared Instrument (MIRI) on board the James Webb Space Telescope (JWST) (Rigby et al. 2023) offers a much higher spectral resolution – $R \sim$ 3000 with the medium-resolution spectrometer (MRS; Argyriou et al. 2023) – and a more than hundredfold gain in sensitivity. This has opened up the exploration of mid-IR molecular lines emitted by the warm gas component in planet-forming disks with an unprecedented accuracy (e.g., Perotti et al. 2023; Grant et al. 2023; Banzatti et al. 2023; Kóspál et al. 2023; Tabone et al. 2023; Arabhavi et al. 2024; Arulanantham et al. 2025; Temmink et al. 2025; Gasman et al. 2025; Kóspál et al. 2025).

As of now, the dust mineralogy aspect with JWST remains largely untapped. Early MIRI studies focusing on dust include Kóspál et al. (2023); Perotti et al. (2023); Jang et al. (2024); Kaeufer et al. (2024b); Grant et al. (2025); Jang et al. (2025); Kóspál et al. (2025); Liu et al. (2025). Most of these studies focused on individual sources rather than on a larger sample. Grant et al. (2025) found an anticorrelation between the strength of the 10 μm silicate feature and the C_2H_2/H_2O line flux ratio, while Arabhavi et al. (2025a) reported that objects with weaker silicate features tend to have higher gas optical depths, traced by

Table 1. Overview of the objects in our sample.

Object	RA (J2000)	Dec (J2000)	SpT	d (pc)	$T_{\rm eff}$ (K)	L_* ($L_\odot$)	Reference
CX Tau	04:14:47.862	26:48:11.014	M1.5	126.7	3487	0.34	(1)
CY Tau	04:17:33.728	28:20:46.812	M1.5	124.3	3516	0.37	(1)
BP Tau	04:19:15.834	29:06:26.926	K5/7	128.2	3777	0.83	(1)
FT Tau	04:23:39.189	24:56:14.250	M2.8	129.9	3415	0.44	(1)
DF Tau	04:27:02.793	25:42:22.453	M3	176.4	3900	3.89	(1)
DL Tau	04:33:39.077	25:20:38.101	K7	159.5	4276	1.47	(1)
DM Tau	04:33:48.734	18:10:09.973	M2	144.8	3715	0.16	(2,3)
AA Tau	04:34:55.420	24:28:53.033	K5	137.7	3762	0.72	(1)
DN Tau	04:35:27.378	24:14:58.910	M1:	127.2	3806	0.69	(1)
LkCa 15	04:39:17.791	22:21:03.390	K5	154.8	4276	1.12	(1)
DR Tau	04:47:06.215	16:58:42.813	K5	186.9	4202	3.71	(1)
RW Aur A	05:07:49.565	30:24:05.131	K0[a]	150.0	4870	0.83	(1,4)
RW Aur B	05:07:49.456	30:24:04.775	K6.5[a]	150.0	4160	0.50	(1,4)
SY Cha	10:56:30.388	–77:11:39.401	K5	180.7	4060	0.43	(1)
TW Hya	11:01:51.905	–34:42:17.033	K6	59.9	4000	0.34	(1)
VW Cha A	11:08:01.482	–77:42:28.567	K7	188.1	4060	2.21	(1,5)
WX Cha A	11:09:58.853	–77:37:08.631	M1	189.3	3710	1.13	(1,5)
XX Cha	11:11:39.673	–76:20:15.032	M3	194.6	3340	0.29	(1)
Sz 50	13:00:55.382	–77:10:22.247	M3	148.9	3400	0.41	(6)
PDS 70	14:08:10.155	–41:23:52.573	K7	112.3	4138	0.38	
GW Lup	15:46:44.729	–34:30:35.677	M1.5	155.2	3632	0.33	(1)
IM Lup	15:56:09.207	–37:56:06.126	M0	153.8	4350	2.57	(1)
Sz 98	16:08:22.494	–39:04:46.427	M0.4	156.2	4060	1.51	(1)
V1094 Sco	16:08:36.177	–39:23:02.464	K6/K5	152.4	4205	1.15	(1)
RNO 90	16:34:09.170	–15:48:16.776	G5	114.9	5662	5.7	(7)
WA Oph 6	16:48:45.633	–14:16:35.849	K6	122.5	4169	2.88	(8)

Notes. This compilation of stellar parameters is based on Henning et al. (2024). Coordinates (ICRS) and spectral types (SpT) are taken from SIMBAD, unless otherwise noted. Distances (d), effective temperatures ($T_{\rm eff}$), and stellar luminosities (L_*) are collected from Gaia DR3 (not noted), (1) Testi et al. (2022), (2) Kenyon & Hartmann (1995), (3) Bertout et al. (2007), (4) Herczeg & Hillenbrand (2014), (5) Daemgen et al. (2013), (6) Sartori et al. (2003), (7) Ghez et al. (1993), and (8) Andrews et al. (2009). [a]Herczeg & Hillenbrand (2014).

the $^{13}CCH_2/C_2H_2$ flux ratio. Tabone et al. (2026) identified four C_2H_2-bright disks (V1094 Sco, DL Tau, CY Tau, and DoAr 33) that also exhibit a strong silica dust component, as revealed by their 9 μm spectral features.

There are two key advantages of MIRI/MRS over Spitzer/IRS for dust studies. First, the higher spectral resolution of MIRI allows for better separation of the solid state features from the molecular lines. Second, the excellent sensitivity of MIRI makes it possible to search for weaker dust components. The Mid-INfrared Disk Survey (MINDS; Henning et al. 2024) is one of the large Guaranteed Time Observations (GTO) programs with JWST/MIRI, and it is aimed at exploring both the gas and dust content in planet-forming disks.

In this work, we present a detailed mineralogy study of the T Tauri subset of the MINDS sample with the aims of (1) determining the dust composition for these disks with a precision surpassing what was possible with Spitzer, (2) searching for less common minerals, and (3) looking for correlations between the mineralogy and the molecular gas chemistry. For the data analysis, we applied spectral decomposition, similar to what was employed in Juhász et al. (2010) for Herbig Ae/Be disks observed with Spitzer/IRS.

The paper is structured as follows. In Sect. 2, we describe the sample and the data. In Sect. 3, we present our model to fit the data along with the dust opacity templates. The results are shown in Sect. 4 and followed by a discussion in Sect. 5. Finally, Sect. 6 provides a summary.

2. Sample and data

The sample of the MINDS GTO program (ID: 1282, PI: Th. Henning, Henning et al. 2024; Kamp et al. 2023) consists of 52 targets, mostly Class II T Tauri objects, but also Herbig Ae disks, and young debris disks. From these, we selected 26 T Tauri disks that are not edge-on and that all show silicate spectral features in emission. Our sample covers spectral types G5–M3, stellar luminosities of 0.16–5.7 $L_\odot$, and distances of 60–195 pc. It also includes the transitional disks LkCa 15, PDS 70, DM Tau, and SY Cha. Table 1 shows an overview of the sample. The objects were observed with MIRI (Rieke et al. 2015; Wright et al. 2015, 2023) in the MRS mode (Wells et al. 2015; Argyriou et al. 2023). The observations, which were taken with a four-point dither pattern using all three grating settings covering the whole 4.9–27.9 μm wavelength range, have been reduced following the same approach as in Temmink et al. (2025). The data were reduced using the standard JWST pipeline reduction (version 1.16.1; Bushouse et al. 2024) with pmap 1315. The spectra were extracted using aperture photometry with the recommended aperture size of 2× the full width at half maximum (FWHM), and residual fringes were corrected using the pipeline's standard implementation.

There are a few known multiple stellar systems in our sample. RW Aur and WX Cha are binaries with separations of 1.5″ and 0.75″, respectively (Daemgen et al. 2013). DF Tau is an equal-mass binary with a semimajor axis of 97 mas (17 au; Allen et al. 2017; Kutra et al. 2025). VW Cha is a quadruple system:

Its component A is a spectroscopic binary with a tentative 10-day period, and the close pair BC is located 0.7″ away from A (Melo 2003; Nguyen et al. 2012; Zsidi et al. 2022). B and C are separated by 0.1″ (Brandeker et al. 2001). Kurtovic et al. (2026) published MIRI spectra of RW Aur, VW Cha, and WX Cha, where they applied special pipeline processing to separate the components in the data. Here we use these component separated spectra of RW Aur A, RW Aur B, VW Cha A, and WX Cha A. We do not study the spectra of VW Cha BC and WX Cha B, because they do not show silicate features. The components of the spectroscopic binary VW Cha A might be so close to each other that they do not possess individual disks. Thus, the IR continuum emission we see in the MIRI data likely originates from a circumbinary disk. In the case of DF Tau, both components have disks, but they are not resolved by JWST (Grant et al. 2024). Since the component spectra cannot be disentangled, the dust composition we derive reflects the average composition of the two disks.

The MRS spectra have a spectral resolution between 1000 and 4000, while the dust features, including the narrower and weaker subpeaks, can already be resolved at a resolving power of $R \sim 30$–50. Since our goal is to model the dust emission, we only require the full spectral resolution to separate the gas lines from the dust continuum. After removing the gas lines, the spectra can therefore be rebinned to a lower resolving power. To achieve this, we applied the following procedure: (1) We smoothed the spectrum using a Savitzky–Golay filter (Savitzky & Golay 1964), with a polynomial degree of three and a variable window length in wavelength space, starting at 0.07 μm at the short-wavelength edge, increasing to 0.11 μm at $\lambda = 10$ μm, and reaching 0.91 μm at the long-wavelength edge[1]. (2) We calculated the residual by subtracting the smoothed spectrum from the original one. (3) We masked all the wavelength locations where the residual values were outside the [0.62%, 93.3%] percentile range. The percentiles were calculated using a ∼1 μm wide rolling window. (4) We repeated the previous steps four more times, updating the mask each time to filter out the remaining spikes. (5) We rebinned the final smoothed spectrum to a lower spectral resolution of $R \approx 100$–200. The advantage of this procedure is its model independence, as it does not require fitting the data with gas or dust spectral templates. This approach works well for our sample of T Tauri disks, where the gas emission is dominated by discrete lines. In contrast, VLMS disks tend to have a molecular pseudo-continuum that cannot be removed with such a procedure (cf. Jang et al. 2025). We also estimated the uncertainties of the data by taking the standard deviation of the non-masked residual values in each bin. However, at wavelengths where the uncertainties provided by the pipeline were larger than our estimates, we kept the original uncertainty values. In this way, we accounted for the inherent uncertainty in the continuum estimation caused by the spectral line residuals.

We did not use the spectral range beyond 27 μm, because of its low signal-to-noise ratio (S/N). There are specific wavelength regions where we noticed that the removal of gas lines were inadequate, for example, 13–15 μm (due to C_2H_2, HCN, and CO_2), 6–7 μm (due to H_2O), and around 26 μm (also due to H_2O). The majority of our spectra are affected by this to varying degrees. To mitigate this issue, we removed the affected spectral regions from our analysis (indicated, e.g., in Fig. 1). Since silicates do not have significant features in these wavelength ranges, this exclusion does not impact our dust analysis.

3. Modeling

3.1. The art of spectral decomposition

The aim of our modeling is to infer the composition, crystallinity, and typical grain sizes of the dust that produces the spectral features in our MIRI spectra. We employed spectral decomposition, which is a widely used approach for interpreting this kind of data. At its core, this technique involves fitting a set of spectral templates, each corresponding to a specific dust component, by linearly combining them with adjustable weights to find the best-fitting result.

The fact that we see the silicate features in emission suggests optically thin radiation that arises from dust in a surface layer warmer than the underlying material, heated by the stellar illumination (e.g., Chiang & Goldreich 1997; Dullemond et al. 2001). However, the combined contribution from the central star and the optically thin emission from micron-sized Mg-silicate grains alone is usually insufficient to account for all the observed thermal IR radiation[2]. The additional featureless IR continuum originates from dust components lacking spectral resonances (such as iron or carbon), or from optically thick dust emission arising in deeper disk layers, or both. We note that the disk's gas is not expected to provide significant continuum emission at these wavelengths. Additionally, polycyclic aromatic hydrocarbons (PAHs), which can be identified by their strong IR spectral bands, can also emit a spectral continuum (Li & Draine 2001). However, we do not detect PAH bands in any of our objects. The directly irradiated sublimation front (hot inner rim of the dusty disk, at $T \sim 1500$ K) can add a distinct continuum emission component which peaks in the near-IR (Dullemond et al. 2001; Natta et al. 2001). To summarize, spectral decomposition models need to include continuum emission sources, and the inference on the dust composition is therefore only partial (cf. Varga et al. 2024). Constituents with featureless opacity curves could still be identified when they contribute to absorption, but this requires detailed radiative transfer calculations.

There are various implementations for spectral decomposition in the literature. The simpler ones (e.g., van Boekel et al. 2005) assumed a single characteristic temperature for the dust emission, and the flux of the dust components was calculated as

$$F_{\nu,\mathrm{dust}} \propto \sum_i C_i \kappa_{\mathrm{abs,i}} B_\nu\left(T_\mathrm{c}\right), \tag{1}$$

where $B_\nu\left(T_\mathrm{c}\right)$ is the Planck function at the characteristic temperature T_c, $\kappa_{\mathrm{abs,i}}$ is the opacity curve of the dust component i, and C_i is the weighting factor[3] which is proportional to the dust mass in component i. The continuum emission components were represented by single-temperature blackbodies. As a next step in complexity, Olofsson et al. (2010) in their B2C model included two distinct dust populations, a warm and a cold one, responsible for the 10 μm and 20–30 μm spectral features, respectively. Juhász et al. (2009) introduced the two-layer temperature distribution

[1] The window length in pixels was 85 at $\lambda < 22$ μm and 151 at $\lambda \gtrsim 22$ μm. For RW Aur A and DF Tau, we used slightly larger window lengths (113 pixels at $\lambda < 22$ μm and 201 pixels at $\lambda \gtrsim 22$ μm), because their spectra are dominated by stronger molecular lines than those in the other objects. The corresponding window length in wavelength space ranges from 0.09 to 1.2 μm, with a value of 0.15 μm at $\lambda = 10$ μm.

[2] It is because Mg-silicates have very low opacities at $\lambda < 8$ μm wavelengths.

[3] The underlying assumption here is that the emission is optically thin. This model becomes unphysical if $\sum_i C_i \kappa_{\mathrm{abs,i}}$, i.e., the optical depth, becomes larger than 1.

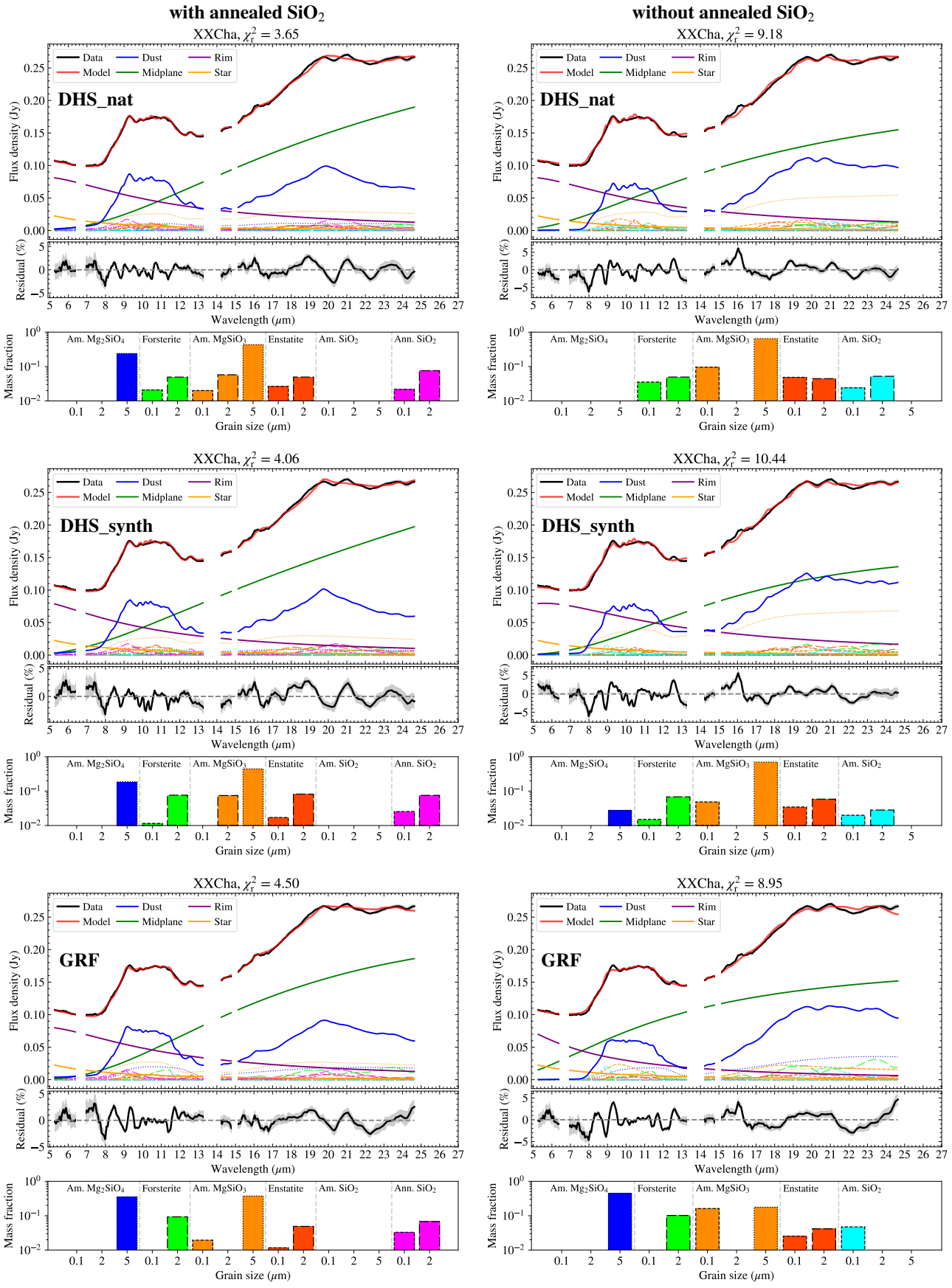

Fig. 1. Fits to the spectrum of XX Cha with the [0.1, 2, 5 am.] grain size set. The panels in the top, middle, and bottom rows show the fits with the DHS_nat, DHS_synth, and GRF sets of opacity curves, respectively. In the left (right) column, fits with (without) annealed SiO_2 are shown. Spectral regions excluded from our fits are not shown.

(TLTD) model, where the emission components, instead of having a single temperature, have power-law temperature distributions. This model can better represent the radially decreasing temperature profile of planet-forming disks. The TLTD model was developed into the TGMdust code in Varga et al. (2024), who used it to fit mid-IR spectro-interferometric data from the VLTI/MATISSE instrument. MIRI spectra show dust spectral features and gas lines in an unprecedented detail, requiring novel analysis methods. Kaeufer et al. (2024a) presented the Dust Continuum Kit with Line emission from Gas (DuCKLinG), which can model both the gas and dust emission at the same time. This unified approach is especially important for VLMS disks, where the molecular lines tend to overpower the dust features, producing a pseudo-continuum (Tabone et al. 2023; Kanwar et al. 2024; Arabhavi et al. 2024; Jang et al. 2025; Kaeufer et al. 2024b).

Circumstellar dust grains likely exist in the form of fractal aggregates composed of multiple different minerals (e.g., Blum & Wurm 2008; Testi et al. 2014). However, it is not yet feasible to take into account the full complexity of the shapes and materials of grains when analyzing IR dust emission, because of computational costs and too many free parameters. Therefore, spectral decomposition techniques require a simplified approach, by defining distinct dust components, each with its own chemical composition, mineralogy, size, and assuming simple grain shapes. Then for each component, a spectral template (opacity, scattering) to be fitted is computed.

3.2. Our `DustComp` model

Our python modeling tool, named `DustComp`[4] is based on Juhász et al. (2009) and Kaeufer et al. (2024a). Our model consists of the following components: central star, inner rim, disk midplane, and disk surface. The central star is represented by a blackbody with an effective temperature ($T_{\rm eff}$) taken from the literature, and an emitting area on the sky calculated from the stellar radius (R_*) and the distance (d) of the source. The stellar radius is estimated from the luminosity (L_*), as reported in the literature. $T_{\rm eff}$, d, and L_* are listed in Table 1. The flux density of the central star is given by

$$F_{\nu,*} = \frac{R_*^2 \pi}{d^2} B_\nu \left(T_{\rm eff}\right). \tag{2}$$

The flux of the central star is fixed in our model. The rim component accounts for the inner rim of the dusty disk that gets direct illumination from the central star, and hence it is the hottest region where dust grains can still exist. We modeled the rim with a single-temperature blackbody ($T_{\rm rim}$) in the shape of an annulus:

$$F_{\nu,\rm rim} = \frac{\pi}{d^2} B_\nu \left(T_{\rm rim}\right) w_{\rm rim} \left(w_{\rm rim} + 2r_{\rm in}\right), \tag{3}$$

where $r_{\rm in}$ is the inner radius of the model disk and $w_{\rm rim}$ is the radial width of the annulus. The corresponding surface area is thus $\pi w_{\rm rim} \left(w_{\rm rim} + 2r_{\rm in}\right)$. The disk midplane component has a power-law radial temperature profile:

$$T_{\rm midplane}\left(r\right) = T_{\rm midplane,in} \left(\frac{r}{r_{\rm in}}\right)^{q_{\rm midplane}}, \tag{4}$$

where $T_{\rm midplane,in}$ is the temperature of the midplane at $r_{\rm in}$, and $q_{\rm midplane}$ is the power-law index. The resulting flux density of the midplane is given by

$$F_{\nu,\rm midplane} = \frac{1}{d^2} \int_{r_{\rm in}}^{r_{\rm out}} 2\pi r B_\nu \left(T_{\rm midplane}\left(r\right)\right) dr. \tag{5}$$

Here $r_{\rm out}$ is the outer radius of the model disk, which we fixed to 20 au, where the dust is too cold to contribute to the emission at MIRI wavelengths. The disk surface component also has a power-law temperature profile:

$$T_{\rm surface}\left(r\right) = T_{\rm surface,in} \left(\frac{r}{r_{\rm in}}\right)^{q_{\rm surface}}, \tag{6}$$

where $T_{\rm surface,in}$ is the temperature of the surface at $r_{\rm in}$, and $q_{\rm surface}$ is the power-law index. To obtain the surface brightness profile, the blackbody source function was multiplied with the weighted sum of the opacities of the dust components:

$$I_{\nu,\rm surface}\left(r\right) = \sum_i C_i \kappa_{\rm abs,i} B_\nu \left(T_{\rm surface}\left(r\right)\right), \tag{7}$$

where C_i are the weights and $\kappa_{\rm abs,i}$ are the opacities. The index i denotes the various dust components, which differ in stoichiometry, grain size, and crystallinity. Here we assume that all dust components share the same radial temperature profile ($T_{\rm surface}$). This is a simplification, as in radiative equilibrium the temperature of a grain depends on its size and optical properties, so different grains located at the same disk radius may have different temperatures. The flux density of the surface component is the following:

$$F_{\nu,\rm surface} = \frac{1}{d^2} \int_{r_{\rm in}}^{r_{\rm out}} 2\pi r I_{\nu,\rm surface}\left(r\right) dr. \tag{8}$$

Finally, the total model flux density was obtained by summing the flux densities of all the components:

$$F_{\nu,\rm model} = F_{\nu,\rm surface} + F_{\nu,\rm midplane} + F_{\nu,\rm rim} + F_{\nu,*} \tag{9}$$

Our model assumes that the relative abundances of the dust components are the same everywhere in the disk. We know from previous studies that the dust composition can in fact change with radius (e.g., van Boekel et al. 2004; Olofsson et al. 2009; Varga et al. 2024). However, we refrain from testing this here, and it will be addressed in another study.

3.3. Dust opacities

Laboratory measurements provide optical data of cosmic dust analogs, from which one can derive spectral templates for the compositional fits. Most of the laboratory optical data are available as complex refractive indices measured on bulk materials (e.g., Jäger et al. 1994; Dorschner et al. 1995; Henning & Mutschke 1997; Zeidler et al. 2015). Absorption and scattering efficiencies can be computed from these data, by taking into account the grain size and applying a grain shape model. Alternatively, laboratory-measured absorption spectra of micron-sized dust particles are also available (e.g., Hallenbeck et al. 1998; Tamanai et al. 2006).

Despite the enormous variety of minerals on Earth and in the Solar System, only a handful have been detected in circumstellar environments (Tielens 2022). Thus, a carefully selected small set of materials may be able to describe our data.

[4] The code, along with the opacity data, is publicly available at `https://github.com/jvarga42/DustComp`

Table 2. Overview of the dust optical data used in this work.

Species	DHS_synth set	DHS_nat set	GRF set
Amorphous Mg_2SiO_4	Jäger et al. (2003)	Jäger et al. (2003)	Henning & Stognienko (1996)
Crystalline forsterite	Suto et al. (2006)[a]	Zeidler et al. (2015)[b,†]	Servoin & Piriou (1973)[a]
Amorphous $MgSiO_3$	Dorschner et al. (1995)	Dorschner et al. (1995)	Dorschner et al. (1995)
Crystalline enstatite	Jäger et al. (1998)[c]	Zeidler et al. (2015)[d,†]	Jäger et al. (1998)[c]
Amorphous SiO_2	Kitamura et al. (2007)	Kitamura et al. (2007)	Henning & Mutschke (1997)
Annealed SiO_2	Fabian et al. (2000)[‡]	Fabian et al. (2000)[‡]	Fabian et al. (2000)[‡]

Notes. Formulae: [(a)] Mg_2SiO_4. [(b)] $Mg_{1.72}Fe_{0.2}SiO_4$. [(c)] $MgSiO_3$. [(d)] $Mg_{0.92}Fe_{0.09}SiO_3$. [†]Measured at 300 K. [‡]5-hour annealed sample.

Following earlier studies (e.g., Juhász et al. 2010; Olofsson et al. 2010; Jang et al. 2024), we used in our modeling amorphous Mg-silicates of olivine (Mg_2SiO_4) and pyroxene ($MgSiO_3$) stoichiometry, as well as silica (SiO_2). In addition, we included the crystalline silicates forsterite and enstatite, the Mg-rich end members of the olivine and pyroxene mineral series, together with annealed silica. We do not include materials that lack mid-IR spectral features, such as iron or amorphous carbon, because our data cannot constrain their abundances. Table 2 lists the materials used in our study, with references to the original laboratory experiments that provided the complex refractive index data measured on bulk materials. The actual data were obtained from the Database of Optical Constants for Cosmic Dust[5] compiled by the Laboratory Astrophysics Group of the Astrophysical Institute and University Observatory (AIU) at Jena.

Grain shape has a significant impact on the emission properties of dust. Following Jang et al. (2024), we considered two grain shape models, one is the distribution of hollow spheres (DHS, Min et al. 2005), and the other is the Gaussian random field (GRF, Min et al. 2007). We used `optool` (Dominik et al. 2021) to calculate the DHS opacity curves. The maximum vacuum filling factor ($f_{\max}$) was set to 0.7 for amorphous grains and 0.99 for crystalline grains. This choice follows Juhász et al. (2010), who found empirically that $f_{\max} \approx 0.7$ provides the best agreement with the observed amorphous silicate features, while values close to unity are required for crystalline grains to match their characteristic band positions and shapes (e.g., Min et al. 2005).

Grain size also plays an important role: as grain size increases, the spectral features become weaker, and for grains larger than ∼10 μm, the features are so weak that it is difficult to distinguish their emission from a featureless continuum. For each material, we calculated opacities for six distinct grain sizes between 0.1 and 5 μm. The resulting opacity curves are presented in Fig. A.1. The figure illustrates that crystalline silicate grains produce more pronounced and sharper spectral features compared to their amorphous counterparts. For more information on the grain shape models and on the calculation of opacities, we refer to Jang et al. (2024). An important aim of our modeling is to determine which grain sizes are minimally required to reproduce the MIRI data. Accordingly, we defined six different sets of grain sizes, as shown in Table 3. Motivated by previous studies that did not find evidence of large crystalline grains in Spitzer spectra of disks (e.g., Bouwman et al. 2008), we include a variant of the [0.1, 2, 5] μm grain-size set in which crystalline grains are restricted to sizes of 0.1 and 2 μm only, and thus in the 5 μm size, we have only amorphous grains (denoted as the [0.1, 2, 5 am.] set).

[5] https://www2.astro.uni-jena.de/Laboratory/OCDB/

Table 3. Grain size sets.

Grain sizes (μm)	Note
[0.1, 2]	
[0.1, 1, 2]	
[0.1, 2, 5 am.]	5 μm-size for amorphous species only
[0.1, 2, 5]	5 μm-size for all species
[0.1, 1, 2, 5]	5 μm-size for all species
[0.1, 1, 2, 3, 4, 5]	5 μm-size for all species

From the opacity curves, we constructed three sets, each of which was fitted to the data in separate runs. Each opacity set contains three amorphous (Mg_2SiO_4, $MgSiO_3$, and SiO_2), and three crystalline materials (forsterite, enstatite, annealed silica). Two sets contain opacities with the DHS grain shape model, while the third one (GRF set) includes GRF opacities[6]. Table 2 provides an overview of the selection of optical data for each opacity set. The two DHS sets, named DHS_synth and DHS_nat, differ in the choices for forsterite and enstatite. While the DHS_synth set includes measurements of high-purity synthetic crystals, for the DHS_nat set, we used measurements of natural crystals that also contained a small amount of iron. The GRF set represents pure, iron-free silicates, as does the DHS_synth set. We further note that the presence of irregular-shaped grains with some Fe content was not tested by these opacity sets and grain shape models.

As shown in Fig. A.1, the spectral features of the natural crystals (Zeidler et al. 2015) appear somewhat smoother than those of the synthetic crystals (Jäger et al. 1998; Suto et al. 2006). For example, synthetic forsterite emits quite strong subpeaks at 9.3, 10.4, and 11.9 μm, whereas these peaks in the spectrum of natural forsterite are much more attenuated. By comparison, observations of debris disk spectra with high forsterite content also show gentler features in the 8–13 μm range (Olofsson et al. 2012), more closely resembling the optical data of the natural forsterite sample. For each opacity set, we also defined a variant that excludes annealed SiO_2. Comparing fits with and without annealed SiO_2 allowed us to directly test for its presence. In summary, we have six sets of dust materials (DHS_synth, DHS_nat, and GRF, each with or without annealed SiO_2), and six sets of grain sizes, resulting in a total of 36 opacity sets.

3.4. Fitting approach

In total, we performed 36 fitting runs per object, one for each opacity set. There are seven fitted parameters corresponding

[6] However, since no GRF opacity data were available for annealed silica, we adopted a DHS opacity curve for that instead.

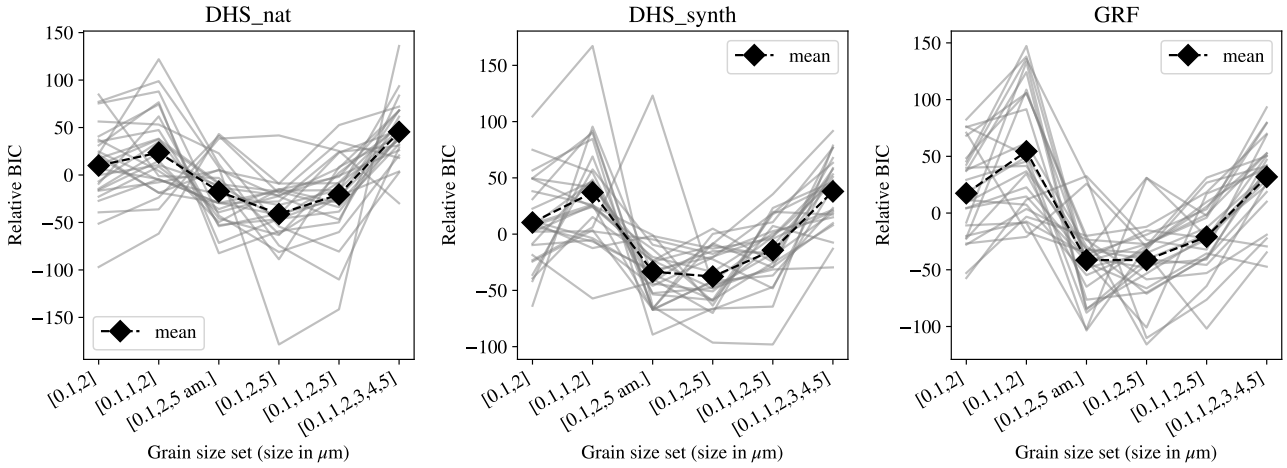

Fig. 2. Relative BIC values for our fits (with opacities including annealed silica) as a function of the grain size sets. The gray lines correspond to individual objects, and the dashed black line is the mean of them. The grain size set [0.1, 2, 5 am.] does not contain 5 μm-sized crystalline grains.

to the disk structure: inner radius ($r_{\rm in}$), the inner temperatures of the disk components ($T_{\rm midplane,in}$, $T_{\rm surface,in}$, $T_{\rm rim}$), the width of the rim ($w_{\rm rim}$), and the power-law gradients of the temperature profiles ($q_{\rm midplane}$, $q_{\rm surface}$). These parameters are optimized with a dynamic nested sampling algorithm (`dynesty`, Higson et al. 2019; Speagle 2020). In each call of the sampler, when the model was evaluated, the weights of the dust components (C_i) were fitted with a nonnegative least squares algorithm (`scipy.optimize.nnls`, Lawson & Hanson 1995). This approach is analogous to what was employed in Juhász et al. (2010) and Jang et al. (2024).

3.5. Differences between `DustComp` and DuCKLinG

`DustComp` is similar in functionality to DuCKLinG (Dust Continuum Kit with Line emission from Gas, Kaeufer et al. 2024a). DuCKLinG can be used to fit both dust spectral features and gas lines, while our tool is limited to fitting dust features. Considering the dust fitting, minor differences between the two tools exist in the parameterization and optimization. In DuCKLinG, the grids are defined in temperature space, while `DustComp` employs radial grids, from which the temperature profile is calculated. Accordingly, `DustComp` uses the inner and outer radii as parameters, while DuCKLinG uses the inner and outer temperatures.

Both tools use nested sampling algorithms for global optimization and a linear least-squares algorithm for spectral decomposition. A further difference is that DuCKLinG performs a normalization prior to the least-squares step, while `DustComp` does not. Finally, DuCKLinG maximizes the full likelihood function, while `DustComp` uses a simplified likelihood that neglects the normalization term.

4. Results

In Fig. 1, as an example, we show the fits for a single object, XX Cha, with the [0.1, 2, 5 am.] grain size set, using the six different opacity sets. Presenting all the 936 fits (6 opacity sets × 6 grain size sets × 26 objects) in the paper would be superfluous. Thus, in the following subsection we perform a quantitative analysis of the fit performance to identify the opacity and grain size sets that provide the globally optimal fit to the data with the smallest number of parameters.

4.1. Selecting the best opacity set

To compare the goodness of fit of the models (with differing number of free parameters), we calculated the Bayesian information criterion (BIC) as

$$\mathrm{BIC} = N_{\rm data} \ln\left(\mathrm{RSS}/N_{\rm data}\right) + N_{\rm free} \ln\left(N_{\rm data}\right), \tag{10}$$

where $N_{\rm free}$ is the number of free parameters (including the weights of the dust components), $N_{\rm data}$ is the number of data points, and RSS is the residual sum of squares between the model and the data, $\mathrm{RSS} = \sum_i^{N_{\rm data}} (D_i - M_i)^2$, D_i being the data values, and M_i being the model values. A lower BIC value indicates a fit improvement that is justified accounting for the increase in the number of free parameters. The BIC can be used to decide whether increasing the number of parameters (such as including more grain sizes) leads to significantly improved fits.

First, we investigated the dependence of the BIC on the grain size sets. For a better comparison, we defined the relative BIC, which is $\mathrm{BIC}_{j,k} - \sum_k^{N_{\rm gs}} \mathrm{BIC}_{j,k}/N_{\rm gs}$, where j, k are the indices of the objects and grain size sets, respectively, and $N_{\rm gs}$ is the number of grain size sets. The average is taken per object, and over the BIC values for the different grain size sets. With this, the inherent differences in the goodness of fit between the objects are removed, and only the impact of the grain size selection is emphasized. In Fig. 2, we plot the relative BIC values for as a function of the grain size sets. For all three opacity sets, we see the same behavior: First, there is no improvement when the number of grains is increased from two to three by adding the 1 μm size. This is illustrated by Fig. A.1, which shows that the opacity curves of 1 μm-sized grains are very similar to those of 0.1 μm-sized grains for most species. However, if we add 5 μm sized grains instead of the 1 μm sized ones, the decrease in the BIC values indicate significantly improved fits.

The lowest average BIC values are obtained with the [0.1, 2, 5] grain-size set for the runs using the DHS_nat and DHS_synth opacity sets. For the GRF opacity set, the [0.1, 2, 5 am.] and [0.1, 2, 5] sets yield nearly identical average BIC values. These two grain-size sets differ only in whether 5 μm-sized crystalline grains are included. There is considerable source-to-source variation in how the BIC changes as a function of the grain-size set, reflecting the mineralogical diversity and thus varying complexity of the spectra in our sample.

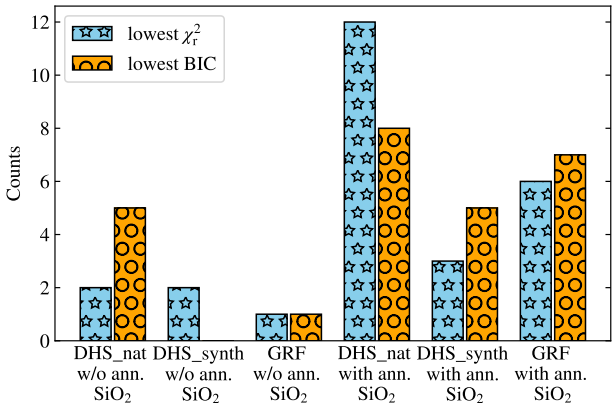

Fig. 3. Bar chart showing how often different opacity sets provide the best fit, as determined by the lowest χ^2_r (orange) or the minimum BIC (blue).

Some spectra may show signatures consistent with large crystalline grains, while others do not; consequently, including large crystalline grains does not lead to a uniform improvement in fit quality across all objects. However, we clearly find that including more than three grain sizes significantly increases the average BIC, indicating that such models are over-parametrized. As a conservative choice, we therefore adopt the [0.1, 2, 5 am.] grain-size set, which does not include large crystalline grains (see also Sect. 5.3).

Next, we compared the fit performance for different choices of opacity set. Fig. 1 presents, for a representative object (XX Cha), the fits obtained with each of the six opacity sets. The figure shows that most of the retrieved mass fractions are consistent across the different opacity choices. One exception is the fraction of the 5 μm-sized amorphous Mg_2SiO_4: When using the DHS_nat opacity set without annealed silica, the fit prefers no 5 μm-sized Mg_2SiO_4. Instead, that fit yields a significantly higher fraction of 5 μm-sized $MgSiO_3$. This behavior indicates a degeneracy between these components, arising from the similarity of their opacity templates. For this reason, the combined mass fraction of large Mg-silicate grains is often a more robust quantity. Further details on these degeneracies are given in Sect. 4.4. Fig. 3 shows how often different opacity sets provide the best fit, based on either the lowest reduced χ square (χ^2_r) or the lowest BIC. From this comparison, the DHS_nat set with annealed silica emerges as a winner. We therefore adopted this opacity set as our preferred choice and present results based on this set in the following.

4.2. Fit results

The fits to the spectra for all objects are shown in Fig. B.1. Overall, the models reproduce the data well, with residuals mostly within ±3%. The χ^2_r values range from 0.5 (DR Tau) to 65 (PDS 70), with a median value of 5.9, indicating statistically significant deviations between the model and the data for most of our targets. The residuals generally show a wavy pattern, with the largest deviations typically occurring around 8, 16, 19, and 21 μm (see also Fig. F.1). The mismatch between the model and the data can be attributed to the following causes: a) the spectral shapes and peak positions of minor subpeaks in the crystalline silicate and silica opacities (Fig. A.1) do not exactly match those in the data, including mismatches in subpeak widths, strengths, and central wavelengths; b) the presence of materials that are not represented in our opacity data; and c) radial variations in dust composition, as our model assumes a homogeneous composition across the entire disk.

Furthermore, for several sources with very high silicate feature amplitudes (e.g., LkCa 15, PDS 70, Sz 98) it is difficult to match the model opacity curves with the data at the short wavelength edge (~8 μm) of the silicate feature. Juhász et al. (2010) showed that deviations of the synthetic spectra from the observations are most likely related to grain shape effects and uncertainties in the iron content of the dust grains. Differences in the data uncertainties among the sample objects also affect the χ^2_r values. For objects exhibiting weaker molecular line emission, the dust continuum is more tightly constrained (cf. Sect. 2), which makes the fits more sensitive to small mismatches and can therefore lead to higher χ^2_r values. From our fits to the MIRI spectra, we derived the mass fraction of each dust component, and the results are listed in Table C.1. The best-fit disk parameters are given in Table D.1. The reported parameter values correspond to the best-fitting solution, while the uncertainties are derived from the 16th–84th percentiles of the equal-weight posterior distributions. We consider a species detected if its mass fraction exceeds 1%.

Our fits reproduce the dust spectra well using Mg-rich (and thus Fe-poor) silicates, in agreement with previous studies (e.g., Bouwman et al. 2008; Olofsson et al. 2009; Juhász et al. 2010). However, we note that opacities of Fe-rich silicates were not included in our fits, and therefore their presence cannot be explicitly ruled out by our analysis. Herschel observations of the 69 μm forsterite feature generally indicate Fe-poor composition, typically containing less than a few percent Fe, although exceptions have also been reported (e.g., Sturm et al. 2013). We also note that our adopted opacity set (DHS_nat) contains some Fe and provides better fits than the other sets (DHS_synth and GRF), which consist of pure synthetic Mg-silicates and silica.

4.3. Comparison with Spitzer/IRS

We performed `DustComp` fits to Spitzer IRS data for several targets in our sample, following the same procedure as for the MIRI data. A comparison for XX Cha is shown in Fig. 4, where the left panel displays the fit to the Spitzer spectrum (AORkey: 12696576, Lebouteiller et al. 2011[7]), and the right panel shows the fit to the MIRI spectrum. Although the shapes of the major dust features is reproduced well in the Spitzer spectrum, the detection of minor dust components, such as silica, is made clear with the improved S/N of the MIRI data. For example, the smaller features that are clearly identifiable in the MIRI spectrum (at 12.6, 16, 19.8, and 21 μm) are barely noticeable, if at all, in the Spitzer spectrum. In the Appendix G, we present a further test where we degrade the MIRI spectrum of XX Cha to simulate Spitzer/IRS low-resolution spectroscopic data. The higher resolving power of MIRI makes it possible to separate the contributions of molecular line emission from those of the dust, which was not feasible with IRS low-resolution spectroscopy. This, and in particular the improvement in S/N, are the main enabling factors for detecting weaker dust constituents in MIRI spectra.

4.4. Degeneracies between dust components

As mentioned in Sect. 4.1, the mass fractions of amorphous species and/or large (≳2 μm) grains can be ambiguous because

[7] The Spitzer spectrum was obtained from the LR7 version of the CASSIS spectral atlas.

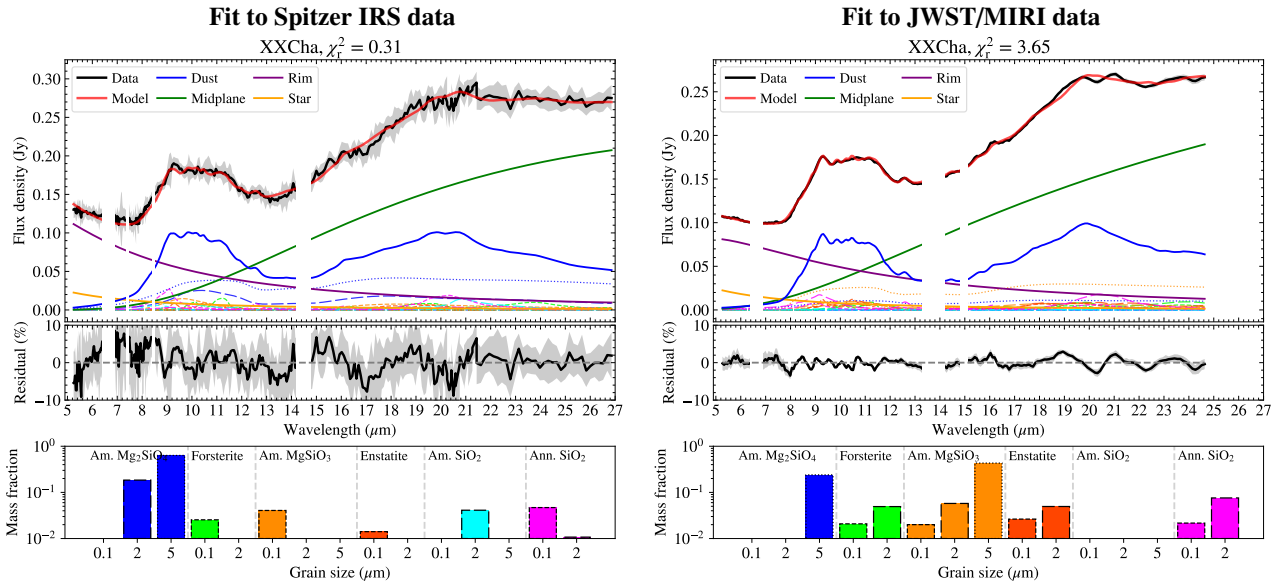

Fig. 4. Comparison of spectral fits for XX Cha using Spitzer (left) and MIRI (right) spectra.

their spectral features are relatively similar, introducing degeneracies in the fitting process. In such cases, the posterior distributions of the corresponding mass fractions often become strongly correlated or multi-modal. We frequently observe that one mode of the posterior favors a solution in which one component of a degenerate pair has a substantial mass fraction while the other is absent, whereas another mode favors the opposite configuration, with intermediate solutions also present. These degeneracies are also reflected in the uncertainties, with the 16th–84th percentile ranges becoming very broad. In these situations, the combined mass fractions of the degenerate components provides a more robust parameter. Typical degenerate pairs include 5 µm-sized Mg_2SiO_4 and 5 µm-sized $MgSiO_3$, as well as the 2 µm and 5 µm grain opacities within a given material. This is illustrated by Fig. A.1, where these opacity curves show similar spectral shapes.

The ambiguities caused by these degeneracies also appear when comparing spectra of the same object with different S/N, such as in the case of XX Cha observed with Spitzer/IRS and MIRI (Fig. 4). In the Spitzer fit, the model favors substantial contributions from both 2 µm and 5 µm-sized Mg_2SiO_4. In contrast, in the MIRI fit only the 5 µm-sized Mg_2SiO_4 component is detected, while 2 µm and 5 µm-sized $MgSiO_3$ grains are present instead. Nevertheless, the combined mass fraction of the 2 µm and 5 µm Mg-silicate grains remains similar between the two fits (82% in the Spitzer fit and 73% in the MIRI fit). This example illustrates that the improved S/N of MIRI does not necessarily resolve the degeneracies between large amorphous grains. Dust components with more distinct opacity curves, such as crystalline grains and 0.1 µm-sized amorphous grains, are much less affected by this degeneracy, and their mass fraction estimates are therefore more reliable. For a more detailed analysis of these degeneracies, we refer to van Boekel et al. (2005) and Sargent et al. (2009b).

An additional factor contributing to these ambiguities is that the opacity decreases with increasing grain size. As a result, large (>2 µm) grains may contribute only weakly to the observed flux despite representing a substantial fraction of the dust mass. For example, if the spectral features can be reproduced either by 2 µm-sized or 5 µm-sized grains of the same material; the latter case requires approximately twice as much mass. Integrated fluxes or luminosities of the dust components therefore may provide a more robust diagnostic since they are largely insensitive to the ambiguity in mass fractions arising from grain-size-dependent opacities.

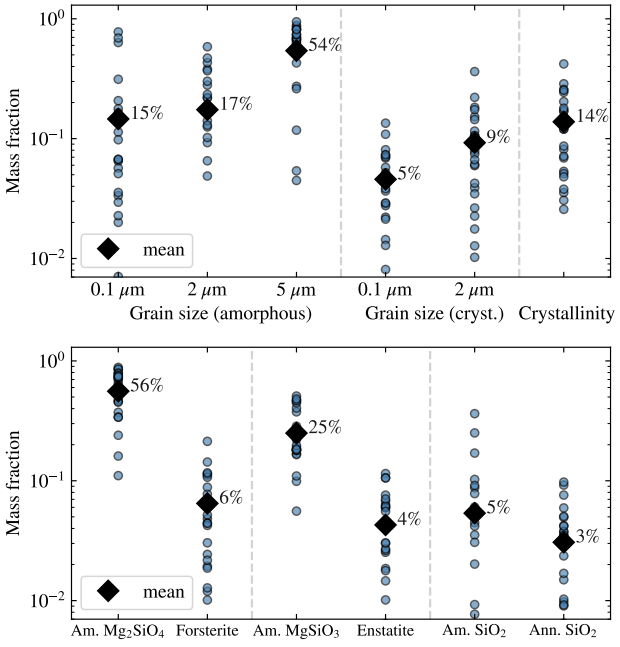

Fig. 5. Top: mass fractions with respect to grain size (separately for the amorphous and crystalline species) and crystallinity. Bottom: mass fractions for the individual dust components. Colored circles represent individual objects, while black diamonds denote the mean values. The numerical percentages indicate these means.

4.5. Sample statistics

Fig. 5 shows mass fractions with respect to grain size, stoichiometry, and crystallinity for the complete sample. Looking

at the sample averages, we see an increasing trend towards larger grain sizes (both for amorphous and crystalline grains), clearly deviating from the Mathis–Rumpl–Nordsieck (MRN) grain size distribution (Mathis et al. 1977) used to describe interstellar dust. Thus, our result on the increased fraction of $\gtrsim$2 μm grains suggest that significant grain growth has happened in the disks of our sample. With regard to stoichiometry, we see that Mg_2SiO_4 (which includes crystalline forsterite and its amorphous counterpart) is the most abundant on average, followed by Mg_2SiO_3. The average value of the crystallinity is 14%, with typical values in the 5–24% range, which is comparable to what was found in earlier studies based on Spitzer spectra (Olofsson et al. 2010; Juhász et al. 2010).

There is growing evidence of significant variability in the IR spectra of planet forming disks (Espaillat et al. 2011; Kóspál et al. 2012; Varga et al. 2017), including variability of the silicate feature (Ábrahám et al. 2009; Bary et al. 2009; Kóspál et al. 2023; Perotti et al. 2023; Jang et al. 2024; Sameshima et al. 2026). Thus, it is plausible that the composition of the dust emitting the IR spectral features changes on observable timescales. Kóspál et al. (2025) analyzed a four-epoch spectral monitoring dataset of the T Tauri source DQ Tau obtained with MIRI between January and March 2025. Their dust compositional fits to each epoch did not reveal significant changes in the dust mineralogy. The IR variability aspect of our MINDS sample will be addressed in a future study.

4.6. Forsterite and annealed silica

Forsterite, which has its main spectral peak at 11.3 μm, is the most commonly found crystalline mineral in planet forming disks. In our sample, the average mass fraction of forsterite is 6.5%, with typical values in the 2–11% range (corresponding to the 16th and 84th percentiles). To enhance the visibility of less abundant dust constituents, we show in the left panel of Fig. 6 the residual dust spectra obtained after subtracting the modeled contributions of the amorphous Mg-silicates and featureless components. These residual spectra therefore emphasize the spectral signatures of crystalline Mg-silicates and silica (both amorphous and annealed). We ordered the spectra to highlight two characteristic groups: one exhibiting strong forsterite features (indicated by a green rectangle), and another showing a well-defined feature at 12.6 μm (indicated by a purple rectangle). We exclude that the 11.3 μm and 12.6 μm are PAH features, since no other PAH bands (e.g., at 6.2 μm or 7.7 μm) can be detected in the data.

Among silicates, the 12.6 μm peak is unique to the annealed silica template. When it is present in the object spectra, it is consistently accompanied by an additional peak at 16.1 μm, moreover, the 20 μm feature exhibits a double-peaked structure, with subpeaks at 19.7 and 20.9 μm. In contrast, forsterite shows bands near 19.5 and 16.3 μm, but does not exhibit prominent features near 12.6 or 20.9 μm. Additionally, sources displaying strong forsterite emission at 11.3 μm show a minor peak at 16.2–16.3 μm, which is clearly offset from the 16.1 μm peak observed in sources that exhibit the 12.6 μm feature. Amorphous (glassy) silica does have a band in the 12–13 μm range; however, this feature is broad and weak compared to the narrow and prominent peak observed here. The prominent 9 μm peak in the data is consistent with both amorphous and crystalline silica templates. Taken together, these characteristics provide strong evidence that the features observed at 12.6, 16.1, and 20.9 μm originate from annealed silica.

This mineral has already been found in a few T Tauri disks Sargent et al. (2009a,b), but the improved S/N of MIRI enables to detect it in a larger fraction of objects (at least 35% within our sample) than was previously possible with Spitzer. The average mass fraction of annealed silica in our sample is 3%, while the highest fraction, 10%, is found in XX Cha.

Most of the residual dust spectra in Fig. 6 show a broad spectral feature between 17 and 23 μm. Although all of our opacity templates show features in this wavelength range, they are not able to precisely reproduce the observed spectra, as the positions of the peaks do not coincide with those seen in the data. A likely explanation for this mismatch is that spectral features in this region are particularly sensitive to the exact grain composition (e.g., iron content) and morphology (Juhász et al. 2010; Jang et al. 2024), and that our opacity set, while sufficient to reproduce the 10 μm feature, lacks the complexity required to do so around 20 μm. Radial variations in dust composition may also contribute to these deviations.

4.7. Relation between the dust and gas content

Thanks to the excellent resolving power and S/N of MIRI, we can now investigate possible relations between the molecular gas content and the dust mineralogy of planet forming disks. In the right panel of Fig. 6, we show the continuum-subtracted spectra in the 13.6–15.1 μm wavelength range. These can be compared to the left panel, which displays the flux contributions from crystalline Mg-silicates and silica (both amorphous and annealed). The figure reveals that most objects showing strong annealed silica features in their dust spectra (highlighted by the purple rectangle) also show relatively strong CO_2 emission lines (with VW Cha A being the only exception). In contrast, objects with prominent forsterite features tend to have relatively strong H_2O emission and weak CO_2 lines. Several sources do not fall into either group; for example, TW Hya and RW Aur B show relatively strong CO_2 emission but weak annealed silica features. Additionally, CY Tau, V1094 Sco, and DL Tau constitute a separate group characterized by strong C_2H_2 emission and similar dust residual spectra indicating a significant fraction of amorphous silica grains. This confirms the finding of Tabone et al. (2026).

Following Gasman et al. (2025), we fitted the continuum-subtracted spectra with slab models to measure line luminosities of CO_2, C_2H_2, and H_2O. For H_2O, we used the pure rotational lines at 23.789–23.912 μm (H_2O_{ro}). In the left panel of Fig. 7, we present the luminosity ratio of CO_2 to H_2O_{ro} as a function of the luminosity ratio of annealed silica to forsterite[8]. As noted in Sect. 4.4, we prefer the luminosity ratios of the dust components over the ratios of their mass fractions, because degeneracies in the mass fractions arising from grain-size-dependent opacities can bias the inferred values. In contrast, feature luminosities provide a more robust diagnostic. We note, however, that luminosity ratios are intrinsically weighted toward smaller grains, which exhibit stronger emission features per unit mass. The figure supports our interpretation that higher CO_2 luminosity (with respect to that of H_2O) is preferentially associated with a larger annealed silica contribution. We observe a very similar trend when annealed silica is replaced by the total silica luminosity.

In the right panel of Fig. 7, we plotted the luminosity ratio of H_2O_{ro} to C_2H_2 as a function of the luminosity ratio of the silica to forsterite. Here we again see a correlation: H_2O-rich

[8] The dust feature luminosities are calculated in the fitted wavelength range of 5–27 μm.

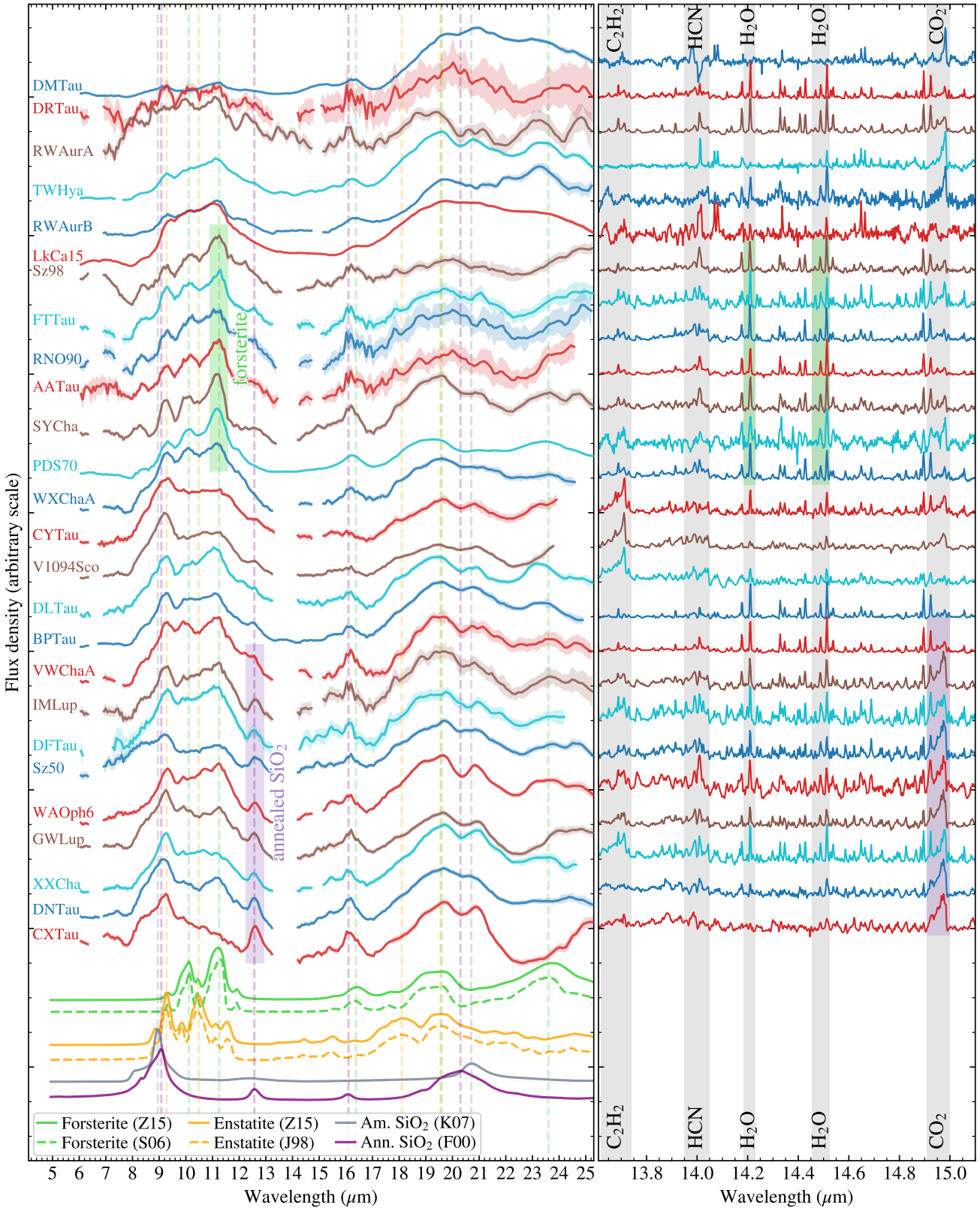

Fig. 6. Left: residual dust spectra after subtracting the modeled contributions of the amorphous Mg-silicates and featureless components. Each residual spectrum has been normalized to its maximum value. The residuals show features of crystalline Mg-silicates and of SiO_2 (both amorphous and annealed). For comparison, at the bottom of the plot, we have plotted the opacity curves of 0.1 μm-sized forsterite, enstatite, amorphous silica, and annealed silica. The positions of major feature peaks are indicated by vertical dashed lines. The green and purple rectangles highlight spectra with prominent features from forsterite and from annealed silica, respectively. Right: continuum-subtracted spectra at full spectral resolution, showing molecular emission lines. The spectra have been normalized to their maximum value within the plotted wavelength range. Most objects showing strong annealed silica features in their dust spectra have relatively strong CO_2 lines, while those with prominent forsterite features tend to be water-rich.

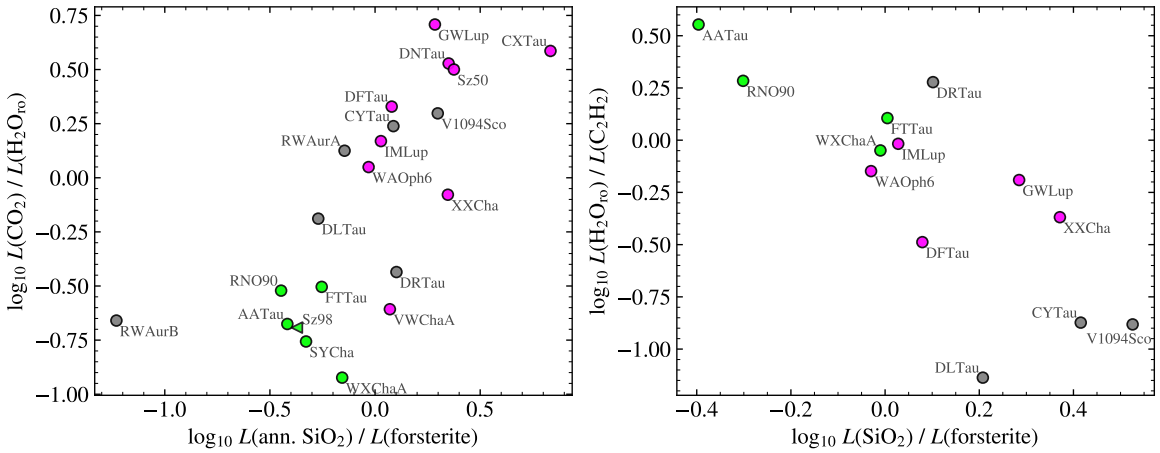

Fig. 7. Left panel: luminosity ratio of CO_2 to H_2O_{ro} versus the luminosity ratio of annealed silica to forsterite. Right panel: luminosity ratio of H_2O_{ro} to C_2H_2 versus the luminosity ratio of the total silica content to forsterite. The purple and green symbols denote objects belonging to the annealed silica-rich and forsterite-rich groups, respectively, identified in Fig. 6. Triangles indicate limits.

and forsterite-rich objects are located in the upper-left part of the diagram, whereas C_2H_2-rich and silica-rich objects lie in the lower-right part. In this case we consider the total silica luminosity, because the trend becomes less clear when only annealed silica is used. The main reason is that the most C_2H_2-rich objects (CY Tau, V1094 Sco, and DL Tau) are not particularly rich in annealed silica but instead show a higher contribution from its amorphous form.

To quantify these trends, we performed linear regression in logarithmic space. For the $L(CO_2)/L(H_2O_{ro})$ diagram we obtained a Pearson correlation coefficient of $\rho = 0.71$ with a p-value of 0.00047. For the $L(H_2O_{ro})/L(C_2H_2)$ plot we got $\rho = -0.79$ with a p-value of 0.0014. Excluding the two leftmost points yields $\rho = -0.58$ with a p-value of 0.098. We therefore conclude that the observed trends are statistically significant. In Sect. 5.5, we discuss the correlation between the dust and molecular gas content in more detail.

5. Discussion

5.1. Grain growth

As can be seen in Fig. A.1, an increase in grain size causes the opacity peaks of silicate minerals to become weaker and flatter. Increased crystallinity can also flatten the shape of the 10 μm feature through the appearance of narrow crystalline subfeatures. Based on these effects, a simple plot showing the 11.3/9.8 μm flux ratio versus the 10 μm feature strength has proven to be a useful diagnostic tool for tracing the degree of dust processing in a wide variety of planet forming disks (Bouwman et al. 2001). In Fig. 8, we present this diagram for our sample[9]. For comparison, we also include corresponding data points for samples of T Tauri and Herbig disks from earlier studies. The data points in the figure are distributed along a line from the upper left to the lower right, indicating that sources with a strong 10 μm silicate emission feature preferentially exhibit a triangular shape which peaking near 9.8 μm (lower right), while sources weaker emission tend to show a flatter silicate feature (upper left). This

[9] Following van Boekel et al. (2003), we normalized the spectra using $1 + (F_\nu - F_{\nu,\mathrm{cont}})/\langle F_{\nu,\mathrm{cont}}\rangle$, where $F_{\nu,\mathrm{cont}}$ is a linear continuum under the 10 μm silicate feature, with anchor points at 7.85 and 13.15 μm. The flux ratio and the feature amplitude are then calculated from this normalized spectrum.

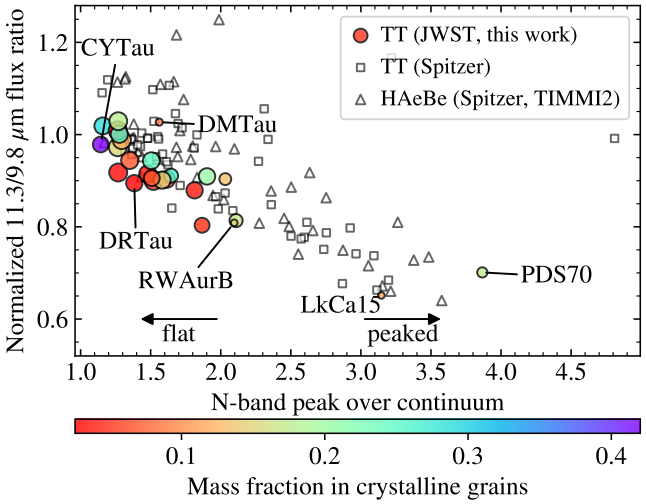

Fig. 8. Normalized 11.3/9.8 μm flux ratio versus the amplitude of the 10 μm silicate feature. Colored circles indicate our new JWST observations. The size of the circles scales with the mass-averaged grain size, while the color indicates the crystallinity ratio. For comparison, corresponding points for samples of Spitzer and TIMMI2 spectra are also plotted (van Boekel et al. 2005; Kessler-Silacci et al. 2006; Juhász et al. 2010).

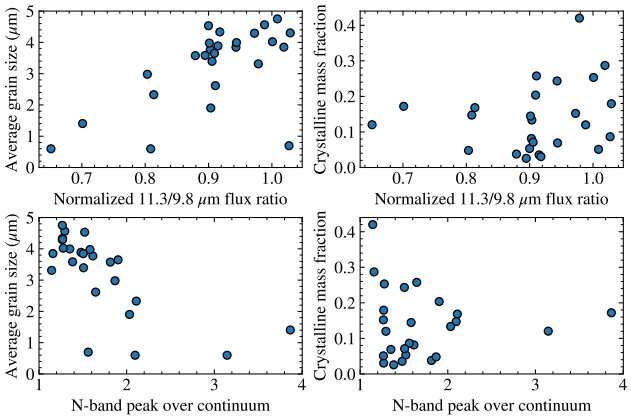

Fig. 9. Scatter plots showing the relationships among the average grain size, crystalline mass fraction, normalized 11.3/9.8 μm flux ratio, and the amplitude of the 10 μm silicate feature.

correlation was first reported by van Boekel et al. (2003) and Przygodda et al. (2003) and has been interpreted as evidence of dust grain growth and increasing crystallinity fraction in disks.

Strong silicate emission with low 11.3/9.8 μm flux ratios is characteristic of small, amorphous grains similar to ISM dust, while weaker and flatter features with higher ratios trace larger grains within the amorphous dust population. Increased crystallinity can also contribute to flattening of the 10 μm feature through narrow crystalline subfeatures superimposed on the broad amorphous silicate emission. In our sample, most objects have relatively flat silicate features, accordingly, their data points are concentrated in the upper left region of the diagram. Our data points overlap with the distributions of the Spitzer and TIMMI2 samples; however, we lack objects showing high amplitude dust emission peaks. The only two objects in our sample occupying this region are LkCa 15 and PDS 70. Since these two are transitional disks, they are considered more evolved than most of our sample. Yet, they occupy the locus where one would expect disks with pristine ISM-like dust. This demonstrates that older systems can still contain dust with "pristine" characteristics, implying that the trend in dust processing cannot be interpreted as a tracer of disk age. A possible explanation for the silicate features in transitional disks is the presence of mechanisms that maintain a population of small, amorphous grains, such as size sorting at an outer pressure bump or secondary generation of small grains in the inner disk.

In Fig. 8, the size of the plot symbols scales with the mass-averaged grain size derived from our spectral decomposition. We indeed find that the fraction of large grains tends to increase toward the upper left part of the figure. In addition, we indicate the crystallinity fraction by color coding. With that, no clear trend is apparent. The relationships between these parameters are further highlighted in Fig. 9. We therefore conclude that increasing grain size, rather than crystallinity, is the primary cause of the observed distribution of data points in the flux ratio versus feature amplitude diagram. This result is in agreement with previous findings from Spitzer data (e.g., Kessler-Silacci et al. 2006; Bouwman et al. 2008).

5.2. PDS 70

PDS 70 has the strongest 10 μm silicate feature with respect to the continuum in our sample. Jang et al. (2024) presented a detailed mineralogical analysis of PDS 70, using a fitting process very similar to ours. Similar to us, they tested different opacity sets for the fits (GRF, DHS, and aerosol), and they found that the data are reproduced best with the GRF set. Our GRF fit to PDS 70 is presented in Fig. E.1. Comparing this to the fit with our adopted DHS_nat opacity set, we find that GRF opacities can better reproduce the features between 16 and 21 μm, while the DHS_nat opacity set reproduces better the 10 μm feature. Overall, we also find, in agreement with Jang et al. (2024), that the GRF set provides a better fit to the MIRI spectrum of PDS 70 than the DHS sets. We also note that our DHS models prefer to have some enstatite, but the GRF models not, which was the same conclusion in Jang et al. (2024). Otherwise, the mass fractions derived from our fits are generally consistent with the ones reported by Jang et al. (2024), despite the different choice of grain sizes. For example, we find a forsterite fraction of 12%, compared to ∼15% in their study. Liu et al. (2025) analyzed the Spitzer and MIRI spectra of PDS 70 using both spectral decomposition and radiative transfer modeling, and their best-fit mass fractions are in good agreement with those we obtained using our DHS_nat opacity set.

5.3. Comparison with Spitzer-based studies

Our findings are in good agreement with earlier mineralogical studies of disks based on Spitzer/IRS data. Consistent with previous work, we find that Mg-rich (and Fe-poor) silicates represent well our data (e.g., Bouwman et al. 2008; Olofsson et al. 2009; Juhász et al. 2010). The crystallinity fractions derived in our analysis, ranging from 3–42%, are also comparable to those reported by Olofsson et al. (2010) for T Tauri disks (mean value 16%) and by Juhász et al. (2010) for Herbig Ae/Be disks (range 1–30%). One notable difference is that we do not require separate warm and cold dust populations to reproduce the observed spectra. This contrasts with the approaches of Bouwman et al. (2008) and Juhász et al. (2010), who modeled narrower wavelength regions by fitting the 10 μm and 20 μm silicate features separately. Similarly, Sargent et al. (2009b) and Olofsson et al. (2010) fitted most of the Spitzer spectral range (5–37 μm) using two dust components, warm and cold, each with its own independent composition. Such analyses led to the so-called crystallinity paradox, suggesting the presence of a compositionally distinct reservoir of cold crystalline material responsible for the longer-wavelength ($\lambda > 20$ μm) silicate bands (Olofsson et al. 2009, 2010).

In our modeling, we adopted a single dust composition across the entire radial and temperature range. Addressing the crystallinity paradox is beyond the scope of this study. Nevertheless, the fact that our model reproduces the spectra very well with a single dust population (with typical root mean square residuals of 1–2%) suggests that compositional differences between the warm ($T \sim 300$–600 K) and cold ($T \sim 100$–200 K) disk regions may be limited. That said, some of the residual features in our fits (Fig. F.1), particularly at wavelengths longer than 18 μm, could be compatible with the presence of cold crystalline material. We also note that our analysis does not cover the 27–35 μm wavelength range included in earlier Spitzer studies, which may provide a more sensitive probe of cold outer disk dust reservoirs.

Previous studies (e.g., Sargent et al. 2009b; Olofsson et al. 2010) derived dust temperatures from their fits to Spitzer spectra. However, a direct comparison with our results is not straightforward because the models employ significantly different parameterizations. While these studies used separate warm and cold dust components, each characterized by a single temperature, our model features radial temperature gradients, such that no single temperature can be uniquely associated with a given emission component. To enable a comparison with previous work, we estimated characteristic temperatures for the dust emission using the following approach. First, we computed the half-flux radius, defined as the radius within which half of the flux at a given wavelength originates. This is a wavelength-dependent quantity. We then evaluated the temperature at the half-flux radius at two selected wavelengths (10 and 23 μm), which can be interpreted as characteristic temperatures of the emission at those wavelengths. We found that at 10 μm the inferred dust temperatures range from 350 to 630 K in our sample (16th–84th percentile range), while at 23 μm they are in the range of 300–500 K. Our 10 μm temperatures are broadly consistent with the warm dust component reported by Sargent et al. (2009b) (490–720 K). In contrast, their cold dust component (110–150 K) is significantly cooler than our inferred temperatures at 23 μm. Both the warm (190–240 K) and cold (60–90 K) dust components

reported by Olofsson et al. (2010) are also significantly cooler than the temperatures inferred in our study and by Sargent et al. (2009b).

Both Bouwman et al. (2008) for T Tauri disks and Juhász et al. (2010) for Herbig Ae/Be disks found that the average size of crystalline grains is smaller than that of the amorphous ones. Other studies, such as Olofsson et al. (2010), did not require large (5–6 µm-sized) crystalline grains to reproduce their spectra. These findings are also supported by theoretical crystallization models (e.g., Gail 2004). A further complication is that the opacity curves of large crystalline grains exhibit significant degeneracy with those of large amorphous grains, making them difficult to distinguish spectroscopically (Olofsson et al. 2010). As described in Sect. 4.1, there is substantial evidence of the presence of large, ∼5 µm-sized amorphous grains in our sample. In contrast, the presence of large crystalline grains is not uniformly supported by our fits; therefore, we did not adopt them in our preferred opacity set. To further examine this issue, we inspected fits obtained with the [0.1, 2, 5] grain-size set, which includes large crystalline grains. This comparison shows that while large crystals are not required in most sources, there are four cases, AA Tau, CY Tau, RNO 90, and Sz 50, where their inclusion noticeably improves the fit.

5.4. Silica mineralogy

Silica occurs in several polymorphic forms that show distinct spectral signatures in the mid-IR (e.g., Koike et al. 2013). The presence of specific silica polymorphs in circumstellar dust can provide insight into the dust's origin, as each polymorph forms under characteristic pressure and temperature conditions. In Fig. 10, we plot the residual spectra after subtracting the modeled contributions of all Mg-silicates and featureless components. The black line is the mean of the residuals in the subset for which annealed silica is robustly detected (highlighted by the purple rectangle in Fig. 6). Our specific choice of silica opacity templates in the modeling could introduce a bias, potentially causing the residual spectra to resemble the adopted opacity profiles. To assess whether this affects our analysis, we performed an additional modeling run in which silica was completely excluded from the opacity set. The resulting average residual spectrum from this run is shown as a dotted line in the figure. We note that the 9 µm peak is significantly weaker in this case, while the other peaks remain in good agreement with those seen in the original residual spectrum. We attribute the reduced strength of the 9 µm feature to the fitting routine attempting to reproduce the silica contribution at this wavelength using enstatite opacity, which also exhibits a prominent band in this region. We therefore conclude that the prominent residual peaks are not artifacts introduced by the adopted opacity set.

To compare the residual peaks with laboratory measurements of cosmic dust analogs, opacity curves of several silica polymorphs, as well as amorphous silica, are shown in Fig. 10. The opacity curve by Fabian et al. (2000), which we have included in our opacity set, is measured on samples which have been annealed at $T \sim 1200$ K from amorphous silica nanoparticles. During the experiment, they observed the appearance of cristobalite and tridymite features in the IR spectra of the samples. Subsequent IR and X-ray diffraction analysis proved cristobalite to be the major component of the annealed silica end product.

The 9.08 µm peak in our data matches all the presented opacity curves; however, the peaks at longer wavelengths allowed us to distinguish between them. The features at 12.58 and 16.1 µm are best matched by cristobalite opacities, while the 20.86 µm

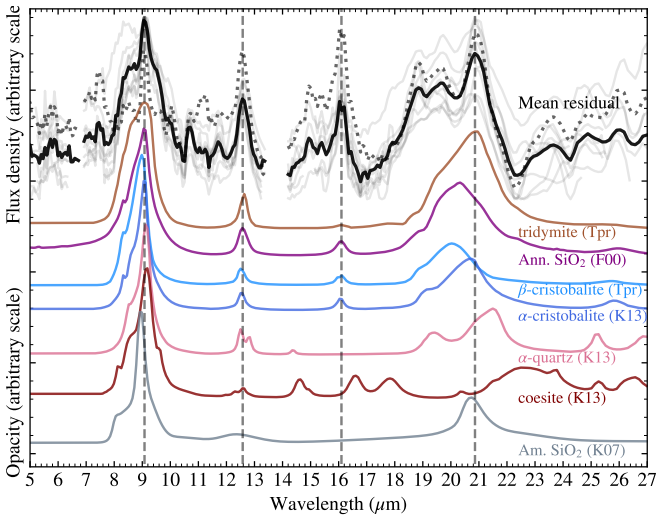

Fig. 10. Upper part: residual spectra obtained after subtracting the modeled contributions of all Mg-silicates and featureless components. Gray lines correspond to individual sources in the subset for which annealed silica is robustly detected. The solid black line shows the average residual spectrum of this subset, highlighting the spectral features of silica. For comparison, the dotted line shows the subset-averaged residuals from a fitting run performed without including any silica opacity templates. Dashed lines indicate the locations of the major spectral peaks in the residuals. Lower part: for comparison, laboratory-measured opacity curves of various silica polymorphs as well as that of amorphous silica are shown. Sources of the opacity data: Tpr: A. Tamanai (priv. comm.), F00: Fabian et al. (2000), K13: Koike et al. (2013), K07: Kitamura et al. (2007).

feature is more consistent with tridymite. We note, however, that other species, such as enstatite and forsterite, also exhibit features around 20 µm, making the identification of this peak with a specific silica polymorph less certain. We therefore conclude that cristobalite is detected as a major component of the annealed silica content in our disk sample, with tridymite also potentially contributing. This is in agreement with the findings of Sargent et al. (2009a) who also found cristobalite as the dominant polymorph of silica in five T Tauri disks. Cristobalite is a high-temperature (forming at $T \gtrsim 1200$ K), low-pressure polymorph, and it was found in chondritic meteorites (Dodd 1981). Furthermore, crystalline silica (predominantly cristobalite) has been found in five out of 25 cometary samples from the Stardust mission (Roskosz & Leroux 2015). Silica, in particular annealed silica, is regarded as a tracer of dust processing because it is not observed in the ISM (Kemper et al. 2004) and is therefore most likely to have formed within planet-forming disks.

Further progress in modeling silica polymorphs will require laboratory measurements of their complex refractive indices, from which opacity curves for arbitrary grain sizes can be computed. Currently, for minerals such as cristobalite, only opacity measurements of powder samples are available, representing a single effective grain size.

5.5. Origin of the dust-gas correlation

Arabhavi et al. (2026) constructed a grid of thermo-chemical models to explore how variations in C and O abundances influence the mid-IR spectra of disks. They identified the molecular flux ratios CO_2/H_2O and H_2O/C_2H_2 as efficient tracers of the C/H and O/H ratios, respectively, and demonstrated that their combination can be used to infer the underlying C/O ratio. In Fig. 11, we reproduce their diagnostic plots and place our objects

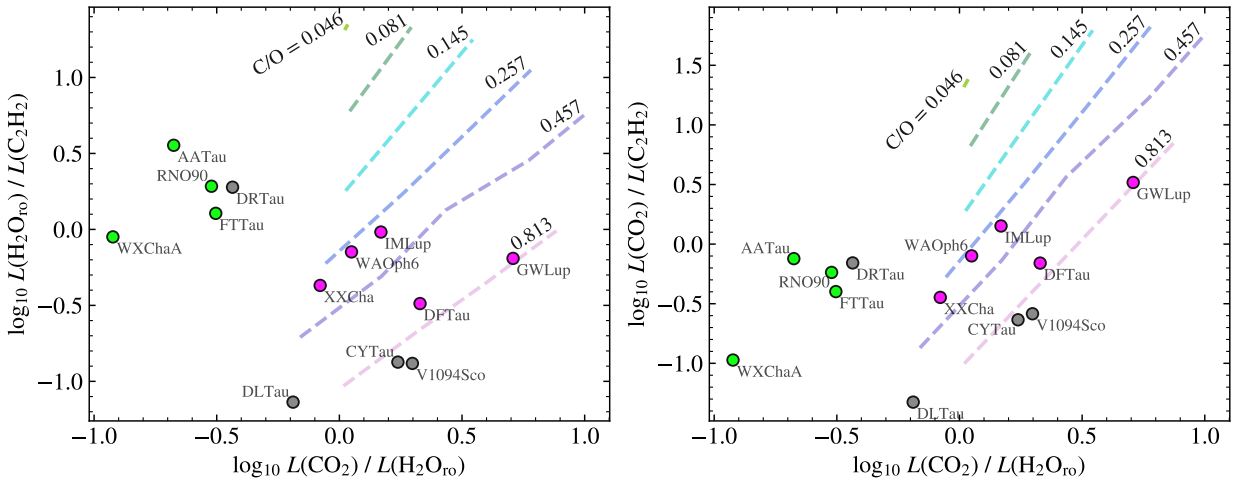

Fig. 11. C/O diagnostic plots following Arabhavi et al. (2026): luminosity ratios H_2O_{ro}/C_2H_2 versus CO_2/H_2O_{ro} (left panel) and CO_2/C_2H_2 versus CO_2/H_2O_{ro} (right panel). The purple and green symbols denote objects belonging to the annealed silica-rich and forsterite-rich groups, respectively, identified in Fig. 6. The dashed lines indicate the C/O ratio derived from the thermo-chemical modeling grid of Arabhavi et al. (2026).

on them. In these plots, the forsterite-rich and annealed silica-rich groups are clearly separated, with the latter located toward the region traced by models with higher C/O ratios. Furthermore, the C_2H_2- and amorphous silica-rich trio of CY Tau, V1094 Sco, and DL Tau is located in the region corresponding to the highest C/O. We therefore suggest that the annealed silica-rich objects in our sample, along with CY Tau, V1094 Sco, and DL Tau, have elevated gas-phase C/O ratios.

This correlation implies some form of coupling between the dust and molecular gas. Thermo-chemical equilibrium calculations of condensates using GGchem (Woitke et al. 2018a; Woitke & Helling 2021) can provide the expected abundances of minerals under the pressure and temperature conditions typical of planet-forming disks. For Solar gas-phase elemental abundances, the equilibrium condensates in the warm and hot inner disk regions ($T > 400$ K) are rich in forsterite and enstatite, while silica is confined to a narrow radial region where $T > 1200$ K (Fig. 9 in Varga et al. 2024). However, we noticed that increasing the C/O ratio makes silica formation more favorable over a broader temperature range. For example, at C/O ≈ 0.9, silica is a major dust component at $T > 900$ K, while the abundances of forsterite and enstatite are correspondingly reduced in these regions. The underlying reason is that increasing the carbon abundance alters the gas-phase chemistry by binding a larger fraction of oxygen into CO, thereby reducing the amount of free oxygen available for silicate formation (e.g., Larimer 1975). This suppresses the formation of Mg-rich silicates, which require relatively large amounts of oxygen, while making silica formation more favorable.

This implies that an increasing gas-phase C/O ratio enhances the silica-to-forsterite and silica-to-enstatite abundance ratios, consistent with what we inferred from the C/O diagnostic plots. Taken together, these results suggest that a process operating in the inner disk regions ($T \gtrsim 400$ K) establishes thermo-chemical equilibrium between the gas and solid phases. One possible mechanism is dust sublimation and subsequent recondensation near the silicate sublimation front, which could bring the gas and dust in the inner disk close to chemical equilibrium. In support of this idea, Kanwar et al. (2025) investigated thermodynamic equilibrium in the inner disk using GGchem and thermo-chemical models and concluded that the very inner disk, close to the dust inner rim, can approach thermodynamic chemical equilibrium.

It remains unclear whether elevated gas-phase C/O ratios are primarily driven by carbon enrichment or by oxygen depletion. Depletion of gas-phase oxygen may occur if water becomes locked in planetesimals that efficiently form just outside the water snowline (Tabone et al. 2023). We note that thermo-chemical models (e.g., Woitke et al. 2018b; Arabhavi et al. 2026) show that CO_2 fluxes are particularly sensitive to the O/H abundance ratio because CO_2 contains two oxygen atoms. Consequently, oxygen depletion would reduce the CO_2 flux more strongly than the H_2O flux. Alternatively, destruction of carbon dust grains provides another pathway for increasing the gas-phase C/O ratio (e.g., Houge et al. 2025; Borderies et al. 2025; Raul et al. 2025). Tabone et al. (2026) also proposed that silica could form in a high gas-phase C/O environment, and they offered an explanation for the elevated C_2H_2/H_2O flux ratios observed in the disks of V1094 Sco and DL Tau. In their scenario, a reduced delivery of water-rich icy pebbles from the outer disk, combined with the advection of chemically evolved gas with an elevated C/O ratio, leads to carbon enrichment in the inner disk regions of these objects.

Pressure bumps associated with rings and gaps may slow or halt radial pebble drift, leading to local dust accumulation and altering the transport of solids to the inner disk (e.g., Pinilla et al. 2012). Such substructures are commonly observed in ALMA images (e.g., Huang et al. 2018), yet their precise impact on the flow of molecular gas and volatile material to the inner disk remains actively debated (e.g., Banzatti et al. 2023; Arulanantham et al. 2025; Gasman et al. 2025; Krijt et al. 2025). In a recent study, Mallaney et al. (2026) reported a dichotomy between molecule-rich and molecule-poor millimeter dust cavities, showing that hydrocarbon-rich chemistry is more prevalent in full disks than in disks with large cavities. Similarly, Gasman et al. (2025) analyzed a sample of disks dominated by gapped millimeter substructures and found that when a substructure is located within the CO and CH_4 snowlines, most disks show detectable mid-IR emission from carbon-bearing species. In contrast, disks with large cavities or very wide gaps tend to show stronger cold water emission and weaker warm water emission. Meanwhile, Volz et al. (2026) reported a transition disk with particularly rich hydrocarbon chemistry. Although we do not explore these correlations in detail, we note that a significant fraction of our forsterite-rich objects (their spectra are

highlighted by a green rectangle in Fig. 6) possess millimeter cavities, including LkCa 15, SY Cha, and PDS 70. These sources also belong to the group we associate with relatively strong water emission. Conversely, the group characterized by prominent annealed silica and CO_2 emission shows no known millimeter cavities in most cases. On a related note, dust substructures in the inner few au disk region, co-located with the gas probed by MIRI, may also strongly influence the molecular chemistry, as demonstrated by Vlasblom et al. (2024) using thermo-chemical modeling. Infrared interferometers, such as the VLTI, are capable of resolving these regions at sub-astronomical-unit spatial resolution (e.g., Varga et al. 2024), thereby directly probing inner-disk substructures.

5.6. Comparison with VLMS disks

As reported by Arabhavi et al. (2025b,a); Grant et al. (2025), MIRI spectra of VLMS disks typically show weak water lines but strong C_2H_2 emission. Grant et al. (2025) suggested that this C_2H_2 enhancement is driven by an increase in the volatile C/O ratio, potentially caused by enrichment in carbon-rich gas rather than by oxygen depletion. In contrast, detailed thermo-chemical modeling of the VLMS disk J1605 indicated that oxygen depletion is the favored scenario to reproduce all observed molecular fluxes (Kanwar et al. 2026). Considering both the MINDS VLMS and T Tauri samples, Grant et al. (2025) identified an anticorrelation between the C_2H_2/H_2O line flux ratio and the strength of the 10 μm silicate feature: sources with weaker silicate features tend to show stronger C_2H_2 emission.

Jang et al. (2025) presented a detailed mineralogical analysis of VLMS disks from the MINDS survey. They confirmed that VLMS disks generally display weaker silicate features than T Tauri disks, although their overall silicate compositions are not fundamentally different. Interpreting the mid-IR spectral slopes, silicate feature strengths, and derived gas column densities within a framework of vertical dust settling, they found that less-settled disks show relatively stronger silicate emission, whereas more-settled disks exhibit higher gas column densities. They noted the presence of a feature near 21 μm in three objects (NC9, HK Cha, and J1605), which resembles silica emission at that wavelength. However, the absence of the accompanying feature at 9 μm makes the detection of silica uncertain.

Grant et al. (2025) and Jang et al. (2025) both suggest that dust in VLMS disks may undergo more rapid vertical settling, thereby exposing deeper disk layers that remain hidden in more massive systems. This would imply that mid-IR observations of VLMS disks probe layers closer to the disk midplane, which may also be present in higher-mass systems but are typically obscured in those disks. This scenario might explain the enhanced presence of carbon-bearing species in VLMS mid-IR spectra. For example, 2D thermo-chemical models indicate that the mid-IR C_2H_2 emitting region lies deeper in the disk than the H_2O emitting region (e.g., Woitke et al. 2018b). Kanwar et al. (2024) also showed this specifically for VLMS disks. Nevertheless, further thermo-chemical modeling is required to robustly test this interpretation. Such modeling should cover a broad stellar mass range, including both VLMS and T Tauri disks, and account for the diversity in the gas-phase C/O ratio as well as the interplay between gas and dust.

6. Summary

We have studied JWST/MIRI spectra of 26 T Tauri disks from the MINDS survey. Compared to Spitzer/IRS, MIRI provides a significant improvement in both S/N ratio and spectral resolving power, enabling the detection of weaker dust features and more precise constraints on dust composition and grain size distribution. For our analysis, we performed spectral decomposition using our new `DustComp` tool, which fits a set of dust opacity templates to the spectra within a flat-disk geometry while assuming emission components with power-law temperature profiles and derives the mass fractions of the individual dust constituents. Following earlier studies, we included amorphous and crystalline Mg-silicates and silica in our opacity set. The opacities were calculated from laboratory measurements of cosmic dust analog materials, assuming the DHS grain-shape model and three representative grain sizes of 0.1, 2, and 5 μm. Our main results are as follows:

- Our fits reproduce the data accurately, with residuals typically within ±3% and root mean square values around 1–2%;
- In agreement with previous studies, we find that Mg-rich (and Fe-poor) silicates represent our spectra very well. However, since Fe-rich silicates were not included in our fits, their presence cannot be explicitly ruled out by our analysis;
- We find strong evidence of the presence of large (∼5 μm) amorphous Mg-silicate grains in our sample objects. However, the presence of large crystalline grains cannot be firmly established. Only in four disks, AA Tau, CY Tau, RNO 90, and Sz 50, does the inclusion of 5 μm-sized crystals noticeably improve the fit quality;
- The dust mass distribution shows an enhanced fraction of $\gtrsim$2 μm grains, clearly deviating from the Mathis–Rumpl–Nordsieck distribution. This indicates that significant grain growth has occurred in the disks of our sample;
- In the 11.3/9.8 μm flux ratio versus 10 μm feature amplitude diagram, we find that the observed trend is primarily driven by increasing grain size rather than crystallinity;
- On average, the dust composition is dominated by grains of Mg_2SiO_4 stoichiometry (∼60%, including amorphous and crystalline state), followed by $MgSiO_3$ (∼30%) and SiO_2 (∼10%) stoichiometries. The average mass fraction of crystalline forsterite is 6.5%, with typical values in the 2–11% range;
- The average crystalline mass fraction is 14%, with typical values between 5 and 24%, in agreement with earlier studies based on Spitzer;
- We robustly detected annealed silica, identified by its characteristic spectral peaks at 12.6, 16.1, and 20.9 μm, in nine out of 26 objects (35%). The average mass fraction of annealed silica is 3%, with the highest value (10%) found in XX Cha. Although this mineral has been previously reported in a few T Tauri disks, the improved S/N of MIRI allowed us to detect it in a larger fraction of objects;
- Having detected silica in our spectra, we further investigated its specific polymorphic forms and found that cristobalite is the dominant component and that tridymite is a potential minor contributor;
- In contrast to previous studies based on Spitzer, we did not require separate warm and cold dust populations to reproduce the observed spectra. This suggests that compositional differences between the warm ($T \sim 300$–600 K) and cold ($T \sim 100$–200 K) disk regions may be limited. Nevertheless, we note that our analysis does not cover the 27–35 μm wavelength range included in earlier Spitzer studies, which provided a more sensitive probe of cold outer disk dust reservoirs;

– We found a correlation between dust composition and molecular gas emission: Most objects with strong annealed silica features also exhibit relatively strong CO_2 emission, whereas objects with prominent forsterite features tend to show strong H_2O emission and weak CO_2 lines;
– Using the C/O diagnostics by Arabhavi et al. (2026), we find that our objects with strong annealed silica features as well as CY Tau, DL Tau, and V1094 Sco may have elevated gas-phase C/O ratios;
– The correlation between silica content and C/O ratio suggests a coupling between the dust and molecular gas components. We propose a scenario in which gas and dust approach a thermo-chemical equilibrium such that an increased gas-phase C/O ratio in the warm and hot disk regions ($T >$ 400 K) enhances the silica abundance while reducing that of forsterite. We further suggest that dust sublimation and subsequent recondensation near the silicate sublimation front may be the process driving the gas and dust in the inner disk toward chemical equilibrium.

Acknowledgements. We thank A. Tamanai for providing silica opacity data and C. Jäger for helpful insights on silica. This work is based on observations made with the NASA/ESA/CSA James Webb Space Telescope. The data were obtained from the Mikulski Archive for Space Telescopes at the Space Telescope Science Institute, which is operated by the Association of Universities for Research in Astronomy, Inc., under NASA contract NAS 5-03127 for JWST. These observations are associated with program #1282. The data described here may be obtained from https://dx.doi.org/10.17909/g10s-6e67.The following National and International Funding Agencies funded and supported the MIRI development: NASA; ESA; Belgian Science Policy Office (BELSPO); Centre Nationale d'Etudes Spatiales (CNES); Danish National Space Centre; Deutsches Zentrum fur Luft- und Raumfahrt (DLR); Enterprise Ireland; Ministerio De Economía y Competividad; Netherlands Research School for Astronomy (NOVA); Netherlands Organisation for Scientific Research (NWO); Science and Technology Facilities Council; Swiss Space Office; Swedish National Space Agency; and UK Space Agency. This work received funding from the Hungarian NKFIH OTKA project no. K-147380. This work was also supported by the NKFIH NKKP grant ADVANCED 149943 and the NKFIH excellence grant TKP2021-NKTA-64. Project no. 149943 has been implemented with the support provided by the Ministry of Culture and Innovation of Hungary from the National Research, Development and Innovation Fund, financed under the NKKP ADVANCED funding scheme. This research was supported in part by grant NSF PHY-2309135 to the Kavli Institute for Theoretical Physics (KITP). TH is grateful for the support by the Hungarian Academy of Sciences in the framework of the MTA Distinguished Guest Fellow Scientist Programme 2025 (VK-4_2025). TH acknowledges support from the European Research Council under the Horizon 2020 Framework Program via the ERC Advanced Grant Origins 83 24 28. IK and JK acknowledge funding from H2020-MSCA-ITN-2019, grant no. 860470 (CHAMELEON). IK, AMA, and EvD acknowledge support from grant TOP-1 614.001.751 from the Dutch Research Council (NWO). EvD acknowledges support from the ERC grant 101019751 MOLDISK and the Danish National Research Foundation through the Center of Excellence 'InterCat' (DNRF150). DG would like to thank the Research Foundation Flanders for co-financing the present research (grant number V435622N) and the European Space Agency (ESA) and the Belgian Federal Science Policy Office (BELSPO) for their support in the framework of the PRODEX Programme. OA thanks the European Space Agency (ESA) and the Belgian Federal Science Policy Office (BELSPO) for their support in the framework of the PRODEX Programme. OA is a Senior Research Associate of the Fonds de la Recherche Scientifique – FNRS TK acknowledges support from STFC Grant ST/Y002415/1. NK thanks the Deutsche Forschungsgemeinschaft (DFG) – grant 138 325594231, FOR 2634/2. GP gratefully acknowledges support from the Carlsberg Foundation, grant CF23-0481 and from the Max Planck Society. LMS has received funding from the European Research Council (ERC) under the European Union's Horizon 2020 research and innovation programme (PROTOPLANETS, grant agreement No. 101002188). BT acknowledges support of the Programme National PCMI of CNRS/INSU with INC/INP cofunded by CEA and CNES. MT and MV acknowledge support from the ERC grant 101019751 MOLDISK. This work made use of the Database of Optical Constants for Cosmic Dust created by the Laboratory Astrophysics Group of the AIU Jena, Germany. The Combined Atlas of Sources with Spitzer IRS Spectra (CASSIS) is a product of the IRS instrument team, supported by NASA and JPL. CASSIS is supported by the "Programme National de Physique Stellaire" (PNPS) of CNRS/INSU co-funded by CEA and CNES and through the "Programme National Physique et Chimie du Milieu Interstellaire" (PCMI) of CNRS/INSU with INC/INP co-funded by CEA and CNES. This research has made use of the SIMBAD database, CDS, Strasbourg Astronomical Observatory, France. This research has made use of the VizieR catalogue access tool, CDS, Strasbourg Astronomical Observatory, France (DOI: 10.26093/cds/vizier). This work made use of the online tool WebPlotDigitizer v5.2 (Rohatgi 2024).

References

Ábrahám, P., Juhász, A., Dullemond, C. P., et al. 2009, Nature, 459, 224
Allen, T. S., Prato, L., Wright-Garba, N., et al. 2017, ApJ, 845, 161
Andrews, S. M., Wilner, D. J., Hughes, A. M., Qi, C., & Dullemond, C. P. 2009, ApJ, 700, 1502
Arabhavi, A. M., Kamp, I., Henning, T., et al. 2024, Science, 384, 1086
Arabhavi, A. M., Kamp, I., Henning, T., et al. 2025a, A&A, 699, A194
Arabhavi, A. M., Kamp, I., van Dishoeck, E. F., et al. 2025b, ApJ, 984, L62
Arabhavi, A. M., Kamp, I., van Dishoeck, E. F., et al. 2026, A&A, 708, A82
Argyriou, I., Glasse, A., Law, D. R., et al. 2023, A&A, 675, A111
Arulanantham, N., Salyk, C., Pontoppidan, K., et al. 2025, AJ, 170, 67
Banzatti, A., Pontoppidan, K. M., Carr, J. S., et al. 2023, ApJ, 957, L22
Bary, J. S., Leisenring, J. M., & Skrutskie, M. F. 2009, ApJ, 706, L168
Bertout, C., Siess, L., & Cabrit, S. 2007, A&A, 473, L21
Birnstiel, T. 2024, ARA&A, 62, 157
Blum, J., & Wurm, G. 2008, ARA&A, 46, 21
Borderies, A., Commerçon, B., & Bourdon, B. 2025, A&A, 694, A89
Bouwman, J., Meeus, G., de Koter, A., et al. 2001, A&A, 375, 950
Bouwman, J., Henning, T., Hillenbrand, L. A., et al. 2008, ApJ, 683, 479
Brandeker, A., Liseau, R., Artymowicz, P., & Jayawardhana, R. 2001, ApJ, 561, L199
Brauer, F., Dullemond, C. P., & Henning, T. 2008, A&A, 480, 859
Bushouse, H., Eisenhamer, J., Dencheva, N., et al. 2024, JWST Calibration Pipeline
Chiang, E. I., & Goldreich, P. 1997, ApJ, 490, 368
Daemgen, S., Petr-Gotzens, M. G., Correia, S., et al. 2013, A&A, 554, A43
D'Alessio, P., Calvet, N., & Woolum, D. S. 2005, in Astronomical Society of the Pacific Conference Series, 341, Chondrites and the Protoplanetary Disk, eds. A. N. Krot, E. R. D. Scott, & B. Reipurth, 353
Dodd, R. T. 1981, Meteorites, a petrologic-chemical synthesis
Dominik, C., Min, M., & Tazaki, R. 2021, OpTool: Command-line driven tool for creating complex dust opacities, Astrophysics Source Code Library [record ascl:2104.010]
Dorschner, J., & Henning, T. 1995, A&A Rev., 6, 271
Dorschner, J., Begemann, B., Henning, T., Jäger, C., & Mutschke, H. 1995, A&A, 300, 503
Draine, B. T. 2003, ARA&A, 41, 241
Dullemond, C. P., Dominik, C., & Natta, A. 2001, ApJ, 560, 957
Ebel, D. S. 2006, in Meteorites and the Early Solar System II, ed. D. S. Lauretta, & H. Y. McSween, 253
Espaillat, C., Furlan, E., D'Alessio, P., et al. 2011, ApJ, 728, 49
Fabian, D., Jäger, C., Henning, T., Dorschner, J., & Mutschke, H. 2000, A&A, 364, 282
Fabian, D., Henning, T., Jäger, C., et al. 2001, A&A, 378, 228
Furlan, E., Luhman, K. L., Espaillat, C., et al. 2011, ApJS, 195, 3
Gail, H. P. 2004, A&A, 413, 571
Gail, H.-P., & Sedlmayr, E. 1999, A&A, 347, 594
Gasman, D., Temmink, M., van Dishoeck, E. F., et al. 2025, A&A, 694, A147
Ghez, A. M., Neugebauer, G., & Matthews, K. 1993, AJ, 106, 2005
Glauser, A. M., Güdel, M., Watson, D. M., et al. 2009, A&A, 508, 247
Grant, S. L., van Dishoeck, E. F., Tabone, B., et al. 2023, ApJ, 947, L6
Grant, S. L., Kurtovic, N. T., van Dishoeck, E. F., et al. 2024, A&A, 689, A85
Grant, S. L., Temmink, M., van Dishoeck, E. F., et al. 2025, A&A, 702, A126
Hallenbeck, S. L., Nuth, J. A., & Daukantas, P. L. 1998, Icarus, 131, 198
Harker, D. E., & Desch, S. J. 2002, ApJ, 565, L109
Henning, T. 2010, ARA&A, 48, 21
Henning, T., & Meeus, G. 2011, in Physical Processes in Circumstellar Disks around Young Stars, ed. P. J. V. Garcia, 114
Henning, T., & Mutschke, H. 1997, A&A, 327, 743
Henning, T., & Salama, F. 1998, Science, 282, 2204
Henning, T., & Stognienko, R. 1993, A&A, 280, 609
Henning, T., & Stognienko, R. 1996, A&A, 311, 291
Henning, T., Kamp, I., Samland, M., et al. 2024, PASP, 136, 054302
Herczeg, G. J., & Hillenbrand, L. A. 2014, ApJ, 786, 97
Higson, E., Handley, W., Hobson, M., & Lasenby, A. 2019, Statist. Comput., 29, 891
Höfner, S., & Olofsson, H. 2018, A&A Rev., 26, 1
Honda, M., Kataza, H., Okamoto, Y. K., et al. 2006, ApJ, 646, 1024
Houge, A., Johansen, A., Bergin, E., et al. 2025, A&A, 699, A227

Huang, J., Andrews, S. M., Dullemond, C. P., et al. 2018, ApJ, 869, L42
Jäger, C., Mutschke, H., Begemann, B., Dorschner, J., & Henning, T. 1994, A&A, 292, 641
Jäger, C., Molster, F. J., Dorschner, J., et al. 1998, A&A, 339, 904
Jäger, C., Dorschner, J., Mutschke, H., Posch, T., & Henning, T. 2003, A&A, 408, 193
Jang, H., Waters, R., Kaeufer, T., et al. 2024, A&A, 691, A148
Jang, H., Arabhavi, A. M., Kaeufer, T., et al. 2025, A&A, 703, A53
Juhász, A., Henning, T., Bouwman, J., et al. 2009, ApJ, 695, 1024
Juhász, A., Bouwman, J., Henning, T., et al. 2010, ApJ, 721, 431
Juhász, A., Dullemond, C. P., van Boekel, R., et al. 2012, ApJ, 744, 118
Kaeufer, T., Min, M., Woitke, P., Kamp, I., & Arabhavi, A. M. 2024a, A&A, 687, A209
Kaeufer, T., Woitke, P., Kamp, I., Kanwar, J., & Min, M. 2024b, A&A, 690, A100
Kamp, I., Henning, T., Arabhavi, A. M., et al. 2023, Faraday Discuss., 245, 112
Kanwar, J., Kamp, I., Jang, H., et al. 2024, A&A, 689, A231
Kanwar, J., Woitke, P., Kamp, I., Rimmer, P., & Helling, C. 2025, A&A, 698, A294
Kanwar, J., Kamp, I., Woitke, P., et al. 2026, A&A, 705, A222
Kemper, F., Vriend, W. J., & Tielens, A. G. G. M. 2004, ApJ, 609, 826
Kenyon, S. J., & Hartmann, L. 1995, ApJS, 101, 117
Kessler-Silacci, J., Augereau, J.-C., Dullemond, C. P., et al. 2006, ApJ, 639, 275
Kitamura, R., Pilon, L., & Jonasz, M. 2007, Appl. Opt., 46, 8118
Koike, C., Noguchi, R., Chihara, H., et al. 2013, ApJ, 778, 60
Kóspál, Á., Ábrahám, P., Acosta-Pulido, J. A., et al. 2012, ApJS, 201, 11
Kóspál, Á., Ábrahám, P., Diehl, L., et al. 2023, ApJ, 945, L7
Kóspál, Á., Ábrahám, P., Akimkin, V. V., et al. 2025, A&A, 703, A20
Krijt, S., Banzatti, A., Zhang, K., et al. 2025, ApJ, 990, L72
Kurtovic, N. T., Grant, S. L., Temmink, M., et al. 2026, A&A, 705, A97
Kutra, T., Prato, L., Tofflemire, B. M., et al. 2025, AJ, 169, 20
Larimer, J. W. 1975, Geochim. Cosmochim. Acta, 39, 389
Lawson, C. L., & Hanson, R. J. 1995, Solving Least Squares Problems (Society for Industrial and Applied Mathematics), _eprint: https://epubs.siam.org/doi/pdf/10.1137/1.9781611971217
Lebouteiller, V., Barry, D. J., Spoon, H. W. W., et al. 2011, ApJS, 196, 8
Li, A., & Draine, B. T. 2001, ApJ, 554, 778
Liu, Y., Li, D., Wang, H., et al. 2025, Sci. China Phys. Mech. Astron., 68, 259511
Lodders, K. 2003, ApJ, 591, 1220
Lodders, K., & Fegley, B. 2002, Icarus, 155, 393
Malfait, K., Waelkens, C., Waters, L. B. F. M., et al. 1998, A&A, 332, L25
Mallaney, P., Banzatti, A., Salyk, C., et al. 2026, ApJ, 998, 255
Mathis, J. S., Rumpl, W., & Nordsieck, K. H. 1977, ApJ, 217, 425
Meeus, G., Juhász, A., Henning, T., et al. 2009, A&A, 497, 379
Melo, C. H. F. 2003, A&A, 410, 269
Min, M., Hovenier, J. W., & de Koter, A. 2005, A&A, 432, 909
Min, M., Waters, L. B. F. M., de Koter, A., et al. 2007, A&A, 462, 667
Natta, A., Prusti, T., Neri, R., et al. 2001, A&A, 371, 186
Nguyen, D. C., Brandeker, A., van Kerkwijk, M. H., & Jayawardhana, R. 2012, ApJ, 745, 119
Oliveira, I., Olofsson, J., Pontoppidan, K. M., et al. 2011, ApJ, 734, 51
Olofsson, J., Augereau, J.-C., van Dishoeck, E. F., et al. 2009, A&A, 507, 327
Olofsson, J., Augereau, J. C., van Dishoeck, E. F., et al. 2010, A&A, 520, A39
Olofsson, J., Juhász, A., Henning, T., et al. 2012, A&A, 542, A90
Perotti, G., Christiaens, V., Henning, T., et al. 2023, Nature, 620, 516
Pinilla, P., Birnstiel, T., Ricci, L., et al. 2012, A&A, 538, A114
Przygodda, F., van Boekel, R., Ábrahám, P., et al. 2003, A&A, 412, L43
Raul, E., Alarcón, F., & Bergin, E. A. 2025, ApJ, 982, 155
Rieke, G. H., Ressler, M. E., Morrison, J. E., et al. 2015, PASP, 127, 665
Rigby, J., Perrin, M., McElwain, M., et al. 2023, PASP, 135, 048001
Rohatgi, A. 2024, WebPlotDigitizer (https://automeris.io)
Roskosz, M., & Leroux, H. 2015, ApJ, 801, L7
Salpeter, E. E. 1977, ARA&A, 15, 267
Sameshima, N., Miyata, T., Kamizuka, T., et al. 2026, MNRAS, 548, stag273
Sargent, B. A., Forrest, W. J., Tayrien, C., et al. 2009a, ApJ, 690, 1193
Sargent, B. A., Forrest, W. J., Tayrien, C., et al. 2009b, ApJS, 182, 477
Sartori, M. J., Lépine, J. R. D., & Dias, W. S. 2003, A&A, 404, 913
Savitzky, A., & Golay, M. J. E. 1964, Analyt. Chem., 36, 1627
Servoin, J. L., & Piriou, B. 1973, Physica Status Solidi B Basic Res., 55, 677
Speagle, J. S. 2020, MNRAS, 493, 3132
Sturm, B., Bouwman, J., Henning, T., et al. 2013, A&A, 553, A5
Suto, H., Sogawa, H., Tachibana, S., et al. 2006, MNRAS, 370, 1599
Tabone, B., Bettoni, G., van Dishoeck, E. F., et al. 2023, Nat. Astron., 7, 805
Tabone, B., Temmink, M., Waters, L. B. F. M., et al. 2026, accepted A&A, arXiv e-prints [arXiv:2604.21803]
Tamanai, A., Mutschke, H., Blum, J., & Meeus, G. 2006, ApJ, 648, L147
Temmink, M., Sellek, A. D., Gasman, D., et al. 2025, A&A, 699, A134
Testi, L., Birnstiel, T., Ricci, L., et al. 2014, in Protostars and Planets VI, eds. H. Beuther, R. S. Klessen, C. P. Dullemond, & T. Henning, 339
Testi, L., Natta, A., Manara, C. F., et al. 2022, A&A, 663, A98
Tielens, A. G. G. M. 2022, Front. Astron. Space Sci., 9, 908217
Tielens, A. G. G. M., Waters, L. B. F. M., Molster, F. J., & Justtanont, K. 1998, Ap&SS, 255, 415
Todini, P., & Ferrara, A. 2001, MNRAS, 325, 726
van Boekel, R., Waters, L. B. F. M., Dominik, C., et al. 2003, A&A, 400, L21
van Boekel, R., Min, M., Leinert, C., et al. 2004, Nature, 432, 479
van Boekel, R., Min, M., Waters, L. B. F. M., et al. 2005, A&A, 437, 189
van Boekel, R., Ábrahám, P., Correia, S., et al. 2006, SPIE Conf. Ser., 6268, 62680D
Varga, J., Gabányi, K. É., Ábrahám, P., et al. 2017, A&A, 604, A84
Varga, J., Ábrahám, P., Chen, L., et al. 2018, A&A, 617, A83
Varga, J., Waters, L. B. F. M., Hogerheijde, M., et al. 2024, A&A, 681, A47
Vlasblom, M., van Dishoeck, E. F., Tabone, B., & Bruderer, S. 2024, A&A, 682, A91
Volz, M., Espaillat, C. C., Pittman, C. V., et al. 2026, AJ, 171, 39
Waelkens, C., Waters, L. B. F. M., de Graauw, M. S., et al. 1996, A&A, 315, L245
Watson, D. M., Leisenring, J. M., Furlan, E., et al. 2009, ApJS, 180, 84
Wells, M., Pel, J.-W., Glasse, A., et al. 2015, PASP, 127, 646
Woitke, P., & Helling, C. 2021, GGchem: Fast thermo-chemical equilibrium code, Astrophysics Source Code Library [record ascl:2104.018]
Woitke, P., Helling, C., Hunter, G. H., et al. 2018a, A&A, 614, A1
Woitke, P., Min, M., Thi, W.-F., et al. 2018b, A&A, 618, A57
Wright, G. S., Wright, D., Goodson, G. B., et al. 2015, PASP, 127, 595
Wright, G. S., Rieke, G. H., Glasse, A., et al. 2023, PASP, 135, 048003
Zeidler, S., Mutschke, H., & Posch, T. 2015, ApJ, 798, 125
Zhukovska, S., Henning, T., & Dobbs, C. 2018, ApJ, 857, 94
Zsidi, G., Fiorellino, E., Kóspál, Á., et al. 2022, ApJ, 941, 177

[1] Konkoly Observatory, HUN-REN Research Centre for Astronomy and Earth Sciences, MTA Centre of Excellence, Konkoly-Thege Miklós út 15–17, 1121 Budapest, Hungary
[2] Max-Planck-Institut für Astronomie (MPIA), Königstuhl 17, 69117 Heidelberg, Germany
[3] Department of Astrophysics/IMAPP, Radboud University, PO Box 9010, 6500 GL Nijmegen, The Netherlands
[4] SRON Netherlands Institute for Space Research, Niels Bohrweg 4, 2333 CA Leiden, The Netherlands
[5] Kapteyn Astronomical Institute, Rijksuniversiteit Groningen, Postbus 800, 9700AV Groningen, The Netherlands
[6] Institute of Physics and Astronomy, ELTE Eötvös Loránd University, Pázmány Péter sétány 1/A, 1117 Budapest, Hungary
[7] Department of Astrophysics, University of Vienna, Türkenschanzstr. 17, 1180 Vienna, Austria
[8] STAR Institute, Université de Liège, Allée du Six Août 19C, 4000, Liège, Belgium
[9] Institute of Astronomy, KU Leuven, Celestijnenlaan 200D, 3001 Leuven, Belgium
[10] Max-Planck-Institut für Extraterrestrische Physik, Giessenbachstrasse 1, 85748 Garching, Germany
[11] Earth and Planets Laboratory, Carnegie Institution for Science, 5241 Broad Branch Road, NW, Washington, DC 20015, USA
[12] ETH Zürich, Institute for Particle Physics and Astrophysics, Wolfgang-Pauli-Str. 27, 8093 Zürich, Switzerland
[13] ASTRON, Netherlands Institute for Radio Astronomy, Oude Hoogeveensedijk 4, 7991 PD Dwingeloo, The Netherlands
[14] Department of Physics and Astronomy, University of Exeter, Exeter EX4 4QL, UK
[15] Department of Astronomy, University of Michigan, 1085 South University Avenue, Ann Arbor, MI 48109, USA
[16] Université Paris-Saclay, Université Paris Cité, CEA, CNRS, AIM, 91191 Gif-sur-Yvette, France
[17] Niels Bohr Institute, University of Copenhagen, NBB BA2, Jagtvej 155A, 2200 Copenhagen, Denmark
[18] Université Paris-Saclay, CNRS, Institut d'Astrophysique Spatiale, 91405 Orsay, France
[19] Leiden Observatory, Leiden University, PO Box 9513, 2300 RA Leiden, The Netherlands

Appendix A: Opacity curves

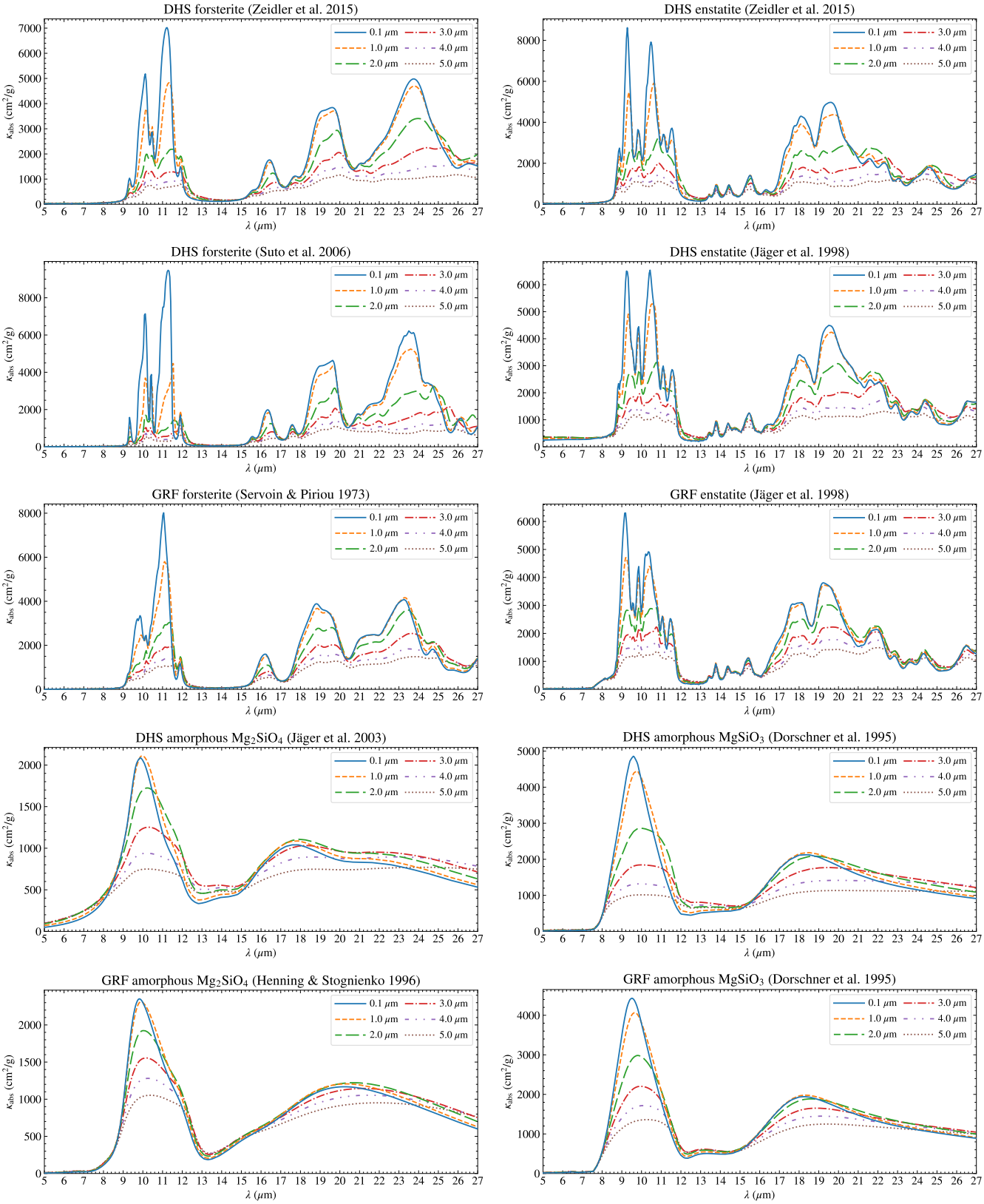

Fig. A.1. Opacity curves used in our modeling.

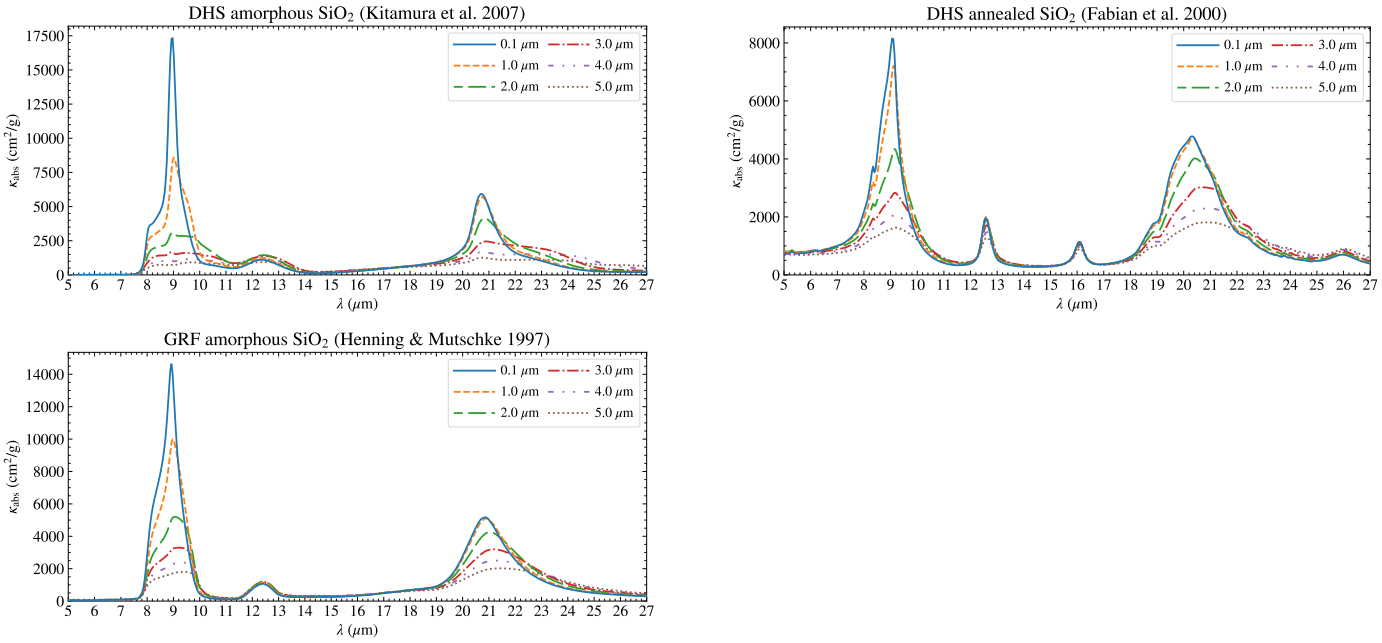

Fig. A.1. continued.

Appendix B: Fit plots

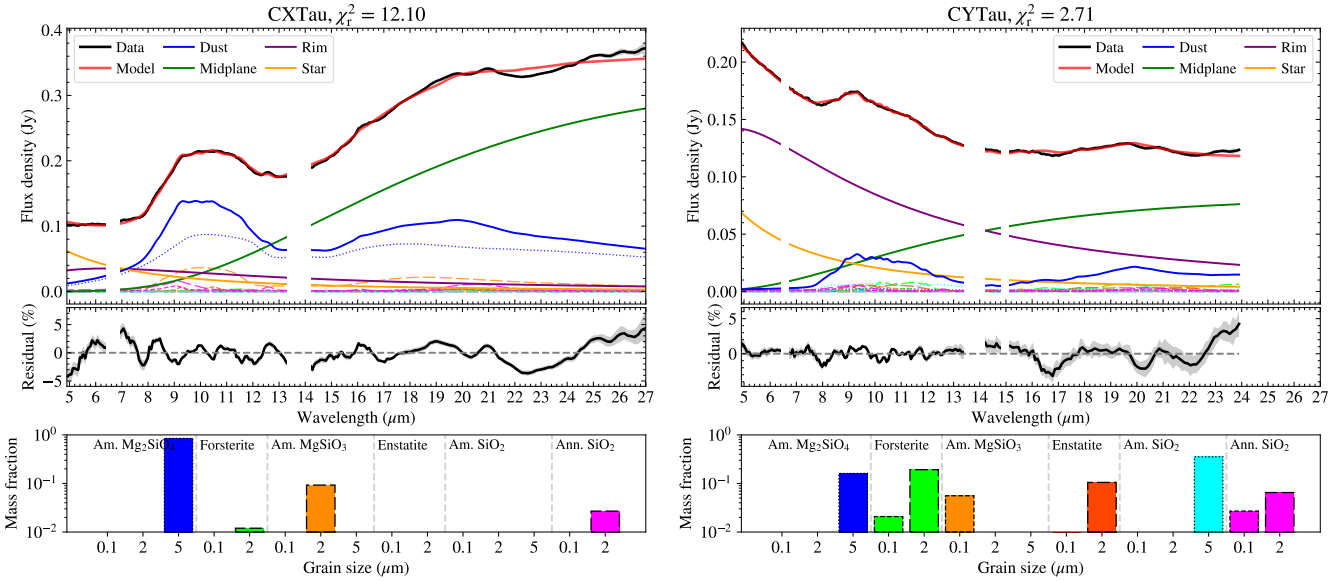

Fig. B.1. Fits to all the spectra, with the DHS_nat set of opacity curves, including annealed silica, using the [0.1, 2, 5 am.] grain size set.

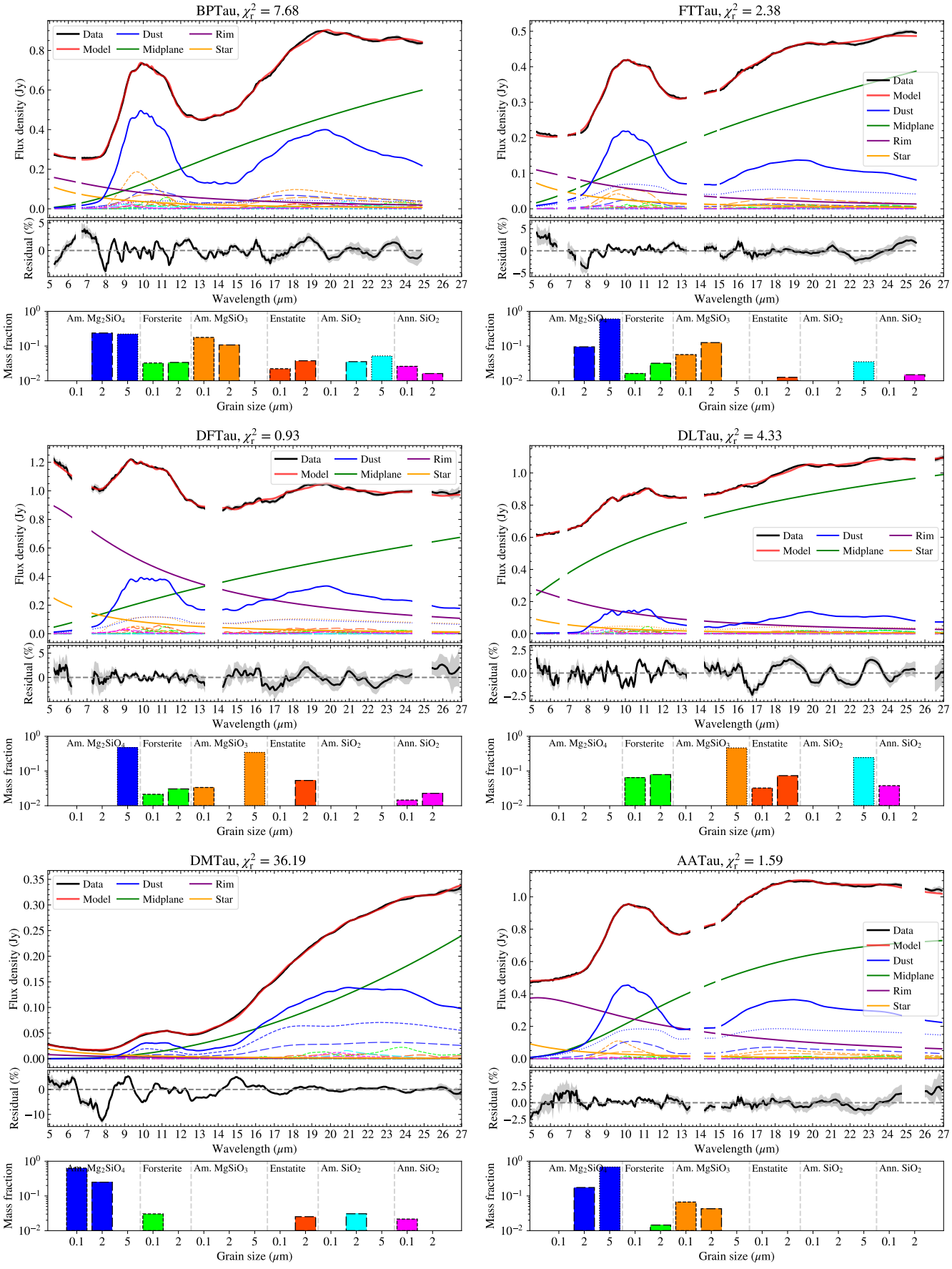

Fig. B.1. continued.

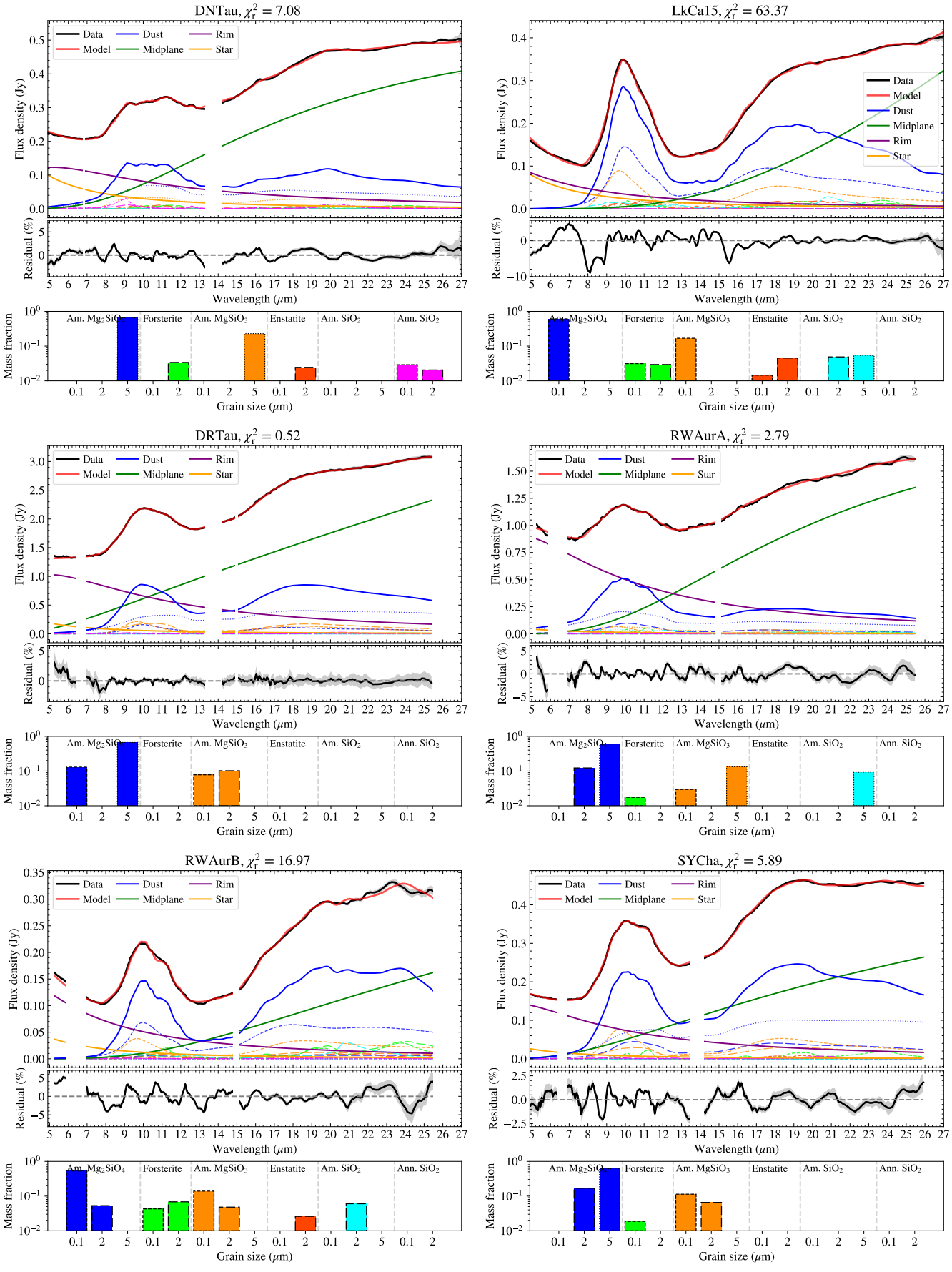

Fig. B.1. continued.

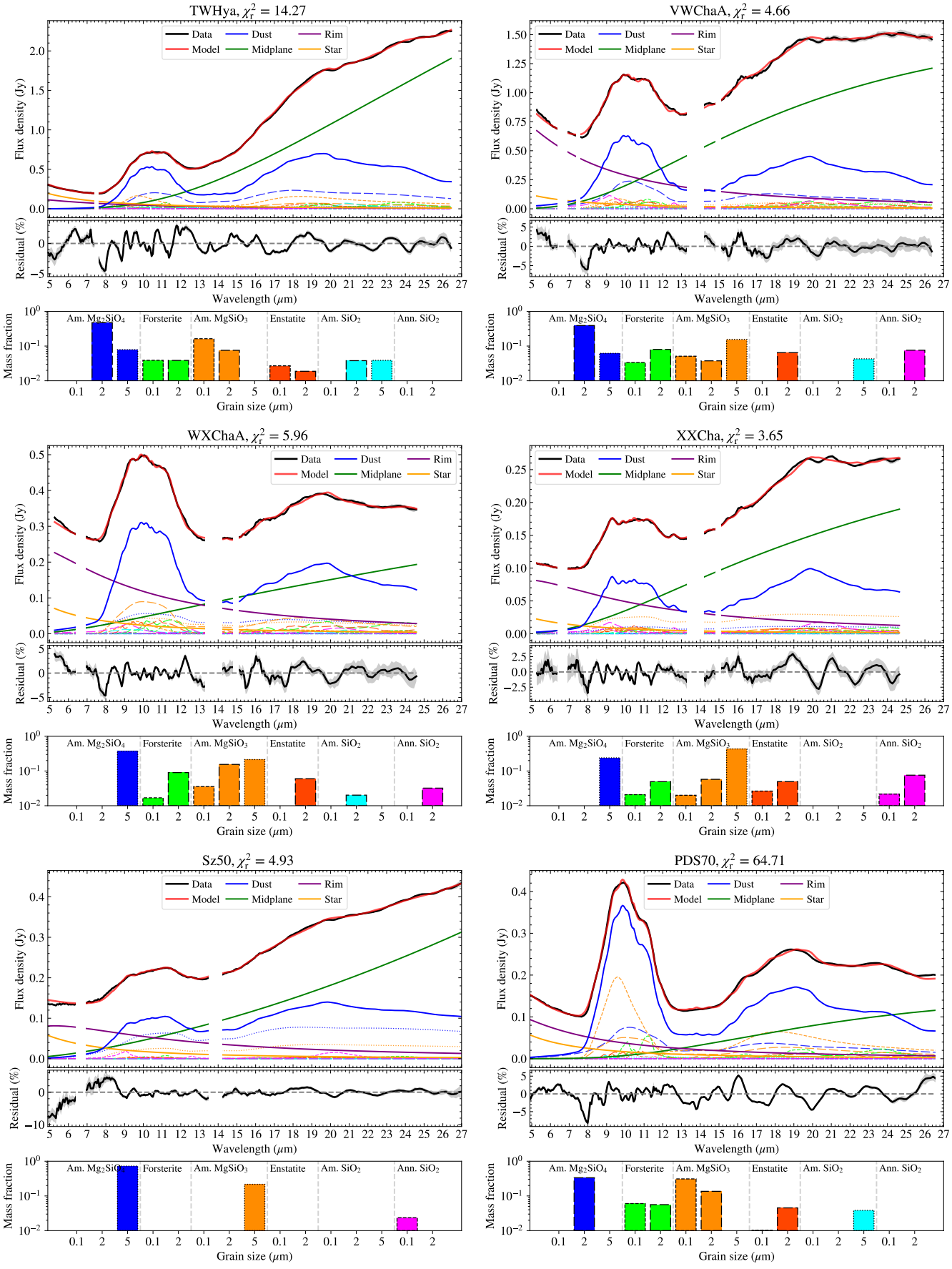

Fig. B.1. continued.

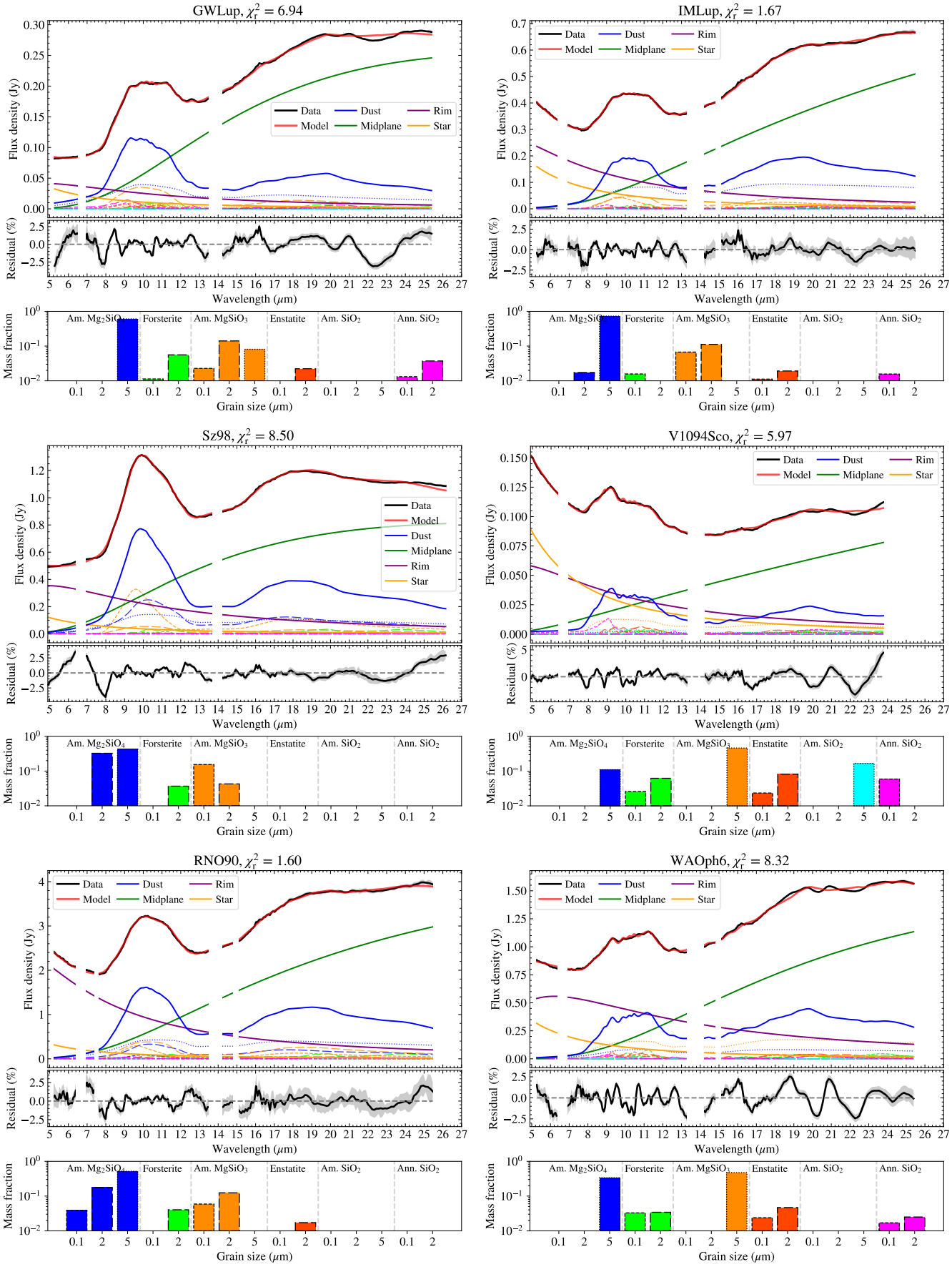

Fig. B.1. continued.

Appendix C: Derived mass fractions.

Table C.1. Mass fractions (%) and χ^2_r values from our fits with the DHS_nat set of opacities. Grain sizes are indicated in μm. Dashes indicate dust species not detected in the fit.

Dust species	Grain size	CX Tau	CY Tau	BP Tau	FT Tau	DF Tau	DL Tau	DM Tau	AA Tau	DN Tau
χ^2_r		12.1	2.7	7.7	2.4	0.9	4.3	36.2	1.6	7.1
Am. Mg_2SiO_4	0.1	–	–	–	$0.00^{+3.15}_{-0.00}$	–	–	$63.4^{+-8.5}_{-26.6}$	$0.00^{+9.84}_{-0.00}$	–
Am. Mg_2SiO_4	2	$0.00^{+5.14}_{-0.00}$	–	$23.8^{+13.3}_{-23.3}$	$9.5^{+24.2}_{-9.5}$	–	–	$24.9^{+-4.6}_{-24.9}$	$17.5^{+17.9}_{-17.5}$	< 0.1
Am. Mg_2SiO_4	5	$84.8^{+0.2}_{-23.0}$	$16.1^{+58.6}_{-16.1}$	$22.1^{+30.2}_{-20.3}$	$60.6^{+8.9}_{-60.6}$	$47.2^{+41.4}_{-47.2}$	$0.00^{+61.22}_{-0.00}$	$0.00^{+54.39}_{-+15.12}$	$68.0^{+16.0}_{-30.0}$	$65.1^{+13.0}_{-21.3}$
Forsterite	0.1	$0.00^{+0.26}_{-0.00}$	$2.1^{+1.7}_{-1.8}$	$3.3^{+0.7}_{-0.9}$	$1.6^{+1.1}_{-0.1}$	$2.1^{+-0.4}_{-2.1}$	$6.4^{+2.6}_{-4.5}$	$3.0^{+-0.5}_{-1.5}$	$0.98^{+0.29}_{-0.56}$	$1.0^{+0.2}_{-0.5}$
Forsterite	2	$1.2^{+3.0}_{-1.2}$	$19.2^{+3.5}_{-18.8}$	$3.4^{+4.5}_{-3.4}$	$3.2^{+9.4}_{-2.2}$	$3.0^{+4.4}_{-3.0}$	$7.9^{+7.5}_{-7.9}$	–	$1.5^{+3.0}_{-1.5}$	$3.4^{+4.3}_{-3.4}$
Am. $MgSiO_3$	0.1	$0.05^{+2.38}_{-0.05}$	$5.6^{+3.8}_{-5.6}$	$17.8^{+2.5}_{-6.1}$	$5.7^{+3.8}_{-3.6}$	$3.4^{+0.2}_{-3.4}$	–	–	$6.7^{+0.9}_{-4.6}$	$0.00^{+1.08}_{-0.00}$
Am. $MgSiO_3$	2	$9.3^{+3.8}_{-5.6}$	–	$10.8^{+4.2}_{-10.8}$	$12.6^{+-1.6}_{-12.6}$	–	–	$0.00^{+0.37}_{-0.00}$	$4.3^{+1.3}_{-4.3}$	$0.00^{+2.69}_{-0.00}$
Am. $MgSiO_3$	5	$0.59^{+14.49}_{-0.59}$	$0.00^{+32.31}_{-0.00}$	$0.00^{+3.28}_{-0.00}$	$0.00^{+24.08}_{-0.00}$	$34.2^{+41.4}_{-34.2}$	$46.2^{+17.2}_{-46.2}$	–	$0.00^{+10.34}_{-0.00}$	$22.9^{+15.8}_{-16.4}$
Enstatite	0.1	$0.64^{+0.27}_{-0.07}$	$0.98^{+0.81}_{-0.98}$	$2.2^{+0.2}_{-0.5}$	$0.59^{+0.43}_{-0.41}$	$0.97^{+-0.04}_{-0.97}$	$3.2^{+1.6}_{-3.1}$	< 0.1	$0.31^{+0.29}_{-0.31}$	$0.17^{+0.30}_{-0.17}$
Enstatite	2	$0.00^{+1.17}_{-0.00}$	$10.5^{+-3.1}_{-10.5}$	$3.8^{+1.4}_{-2.0}$	$1.3^{+3.3}_{-1.1}$	$5.3^{+0.4}_{-5.3}$	$7.4^{+3.9}_{-7.4}$	$2.5^{+-0.6}_{-1.5}$	$0.16^{+1.60}_{-0.16}$	$2.4^{+1.6}_{-2.2}$
Am. SiO_2	0.1	–	$0.90^{+2.42}_{-0.81}$	$0.00^{+0.45}_{-0.00}$	$0.00^{+0.18}_{-0.00}$	$0.00^{+0.38}_{-0.00}$	$0.71^{+2.30}_{-0.71}$	–	< 0.1	< 0.1
Am. SiO_2	2	–	< 0.1	$3.6^{+1.2}_{-3.1}$	–	–	–	$3.1^{+-1.3}_{-2.3}$	–	–
Am. SiO_2	5	–	$35.4^{+-4.8}_{-29.9}$	$5.2^{+7.1}_{-3.9}$	$3.5^{+12.7}_{-3.5}$	–	$24.4^{+4.3}_{-20.3}$	–	$0.00^{+0.32}_{-0.00}$	$0.00^{+4.30}_{-0.00}$
Ann. SiO_2	0.1	$0.79^{+1.22}_{-0.65}$	$2.7^{+-0.8}_{-2.7}$	$2.6^{+-0.2}_{-2.6}$	$0.00^{+0.29}_{-0.00}$	$1.5^{+-0.5}_{-1.5}$	$3.8^{+1.3}_{-3.8}$	$2.2^{+-2.2}_{-2.2}$	$0.00^{+0.51}_{-0.00}$	$2.9^{+1.0}_{-0.8}$
Ann. SiO_2	2	$2.7^{+1.0}_{-1.3}$	$6.5^{+2.9}_{-6.5}$	$1.6^{+1.9}_{-1.6}$	$1.5^{+1.1}_{-1.5}$	$2.3^{+-0.1}_{-2.3}$	–	$0.94^{+2.58}_{-+1.42}$	$0.65^{+0.25}_{-0.65}$	$2.1^{+0.7}_{-2.1}$

Dust species	Grain size	LkCa 15	DR Tau	RW Aur A	RW Aur B	SY Cha	TW Hya	VW Cha A	WX Cha A	XX Cha
χ^2_r		63.4	0.5	2.8	17.0	5.9	14.3	4.7	6.0	3.6
Am. Mg_2SiO_4	0.1	$60.9^{+2.9}_{-1.9}$	$13.0^{+15.0}_{-12.3}$	$0.00^{+7.78}_{-0.00}$	$55.2^{+4.6}_{-5.4}$	$0.00^{+8.83}_{-0.00}$	–	$0.00^{+9.52}_{-0.00}$	$0.00^{+0.37}_{-0.00}$	–
Am. Mg_2SiO_4	2	–	$0.00^{+40.50}_{-0.00}$	$12.3^{+16.8}_{-12.3}$	$5.3^{+1.1}_{-5.3}$	$16.8^{+17.1}_{-16.8}$	$47.1^{+11.2}_{-16.3}$	$39.1^{+3.4}_{-39.1}$	$0.00^{+15.83}_{-0.00}$	$0.00^{+7.77}_{-0.00}$
Am. Mg_2SiO_4	5	–	$66.5^{+4.3}_{-66.5}$	$59.0^{+20.5}_{-59.0}$	$0.00^{+6.67}_{-0.00}$	$61.5^{+12.3}_{-24.7}$	$7.9^{+23.0}_{-7.9}$	$6.2^{+48.7}_{-6.2}$	$37.2^{+21.8}_{-37.2}$	$24.0^{+40.1}_{-24.0}$
Forsterite	0.1	$3.1^{+0.2}_{-0.6}$	$0.39^{+0.39}_{-0.39}$	$1.8^{+0.6}_{-1.5}$	$4.3^{+1.0}_{-1.0}$	$1.9^{+0.2}_{-0.6}$	$3.9^{+0.8}_{-0.6}$	$3.4^{+1.2}_{-0.9}$	$1.7^{+1.2}_{-+0.2}$	$2.1^{+1.3}_{-0.7}$
Forsterite	2	$2.9^{+1.3}_{-1.6}$	$0.62^{+6.38}_{-0.62}$	$0.19^{+7.99}_{-0.19}$	$6.9^{+3.7}_{-4.8}$	$0.00^{+1.78}_{-0.00}$	$3.9^{+1.7}_{-3.2}$	$8.0^{+9.8}_{-6.9}$	$9.0^{+3.1}_{-7.4}$	$4.9^{+6.2}_{-4.9}$
Am. $MgSiO_3$	0.1	$16.8^{+0.4}_{-2.4}$	$7.8^{+9.9}_{-4.2}$	$2.9^{+10.3}_{-2.9}$	$13.9^{+3.5}_{-2.9}$	$11.3^{+2.0}_{-4.9}$	$16.3^{+2.4}_{-3.0}$	$5.1^{+9.7}_{-3.8}$	$3.6^{+3.9}_{-0.7}$	$2.0^{+3.7}_{-2.0}$
Am. $MgSiO_3$	2	–	$10.2^{+2.4}_{-10.2}$	$0.24^{+6.52}_{-0.24}$	$4.8^{+-3.6}_{-4.8}$	$6.6^{+4.6}_{-3.2}$	$7.5^{+4.0}_{-7.5}$	$3.8^{+7.0}_{-3.8}$	$15.5^{+-2.1}_{-15.5}$	$5.8^{+2.2}_{-5.8}$
Am. $MgSiO_3$	5	–	$0.00^{+29.77}_{-0.00}$	$13.3^{+37.2}_{-13.3}$	$0.00^{+9.66}_{-0.00}$	$0.00^{+4.25}_{-0.00}$	–	$15.7^{+15.1}_{-15.7}$	$21.3^{+24.7}_{-8.2}$	$43.2^{+11.9}_{-43.2}$
Enstatite	0.1	$1.4^{+0.4}_{-0.5}$	$0.30^{+0.62}_{-0.30}$	$0.49^{+-0.25}_{-0.49}$	$0.39^{+0.81}_{-0.39}$	$0.78^{+0.19}_{-0.26}$	$2.7^{+0.3}_{-0.8}$	$0.30^{+0.59}_{-0.30}$	$0.14^{+0.59}_{-0.08}$	$2.6^{+0.7}_{-1.0}$
Enstatite	2	$4.5^{+1.0}_{-0.5}$	$0.29^{+3.01}_{-0.29}$	$0.00^{+1.39}_{-0.00}$	$2.6^{+0.6}_{-1.3}$	$0.24^{+0.80}_{-0.24}$	$1.9^{+0.6}_{-0.7}$	$6.5^{+4.5}_{-3.9}$	$6.0^{+2.1}_{-4.2}$	$4.9^{+2.5}_{-4.5}$
Am. SiO_2	0.1	–	$0.00^{+0.36}_{-0.00}$	$0.00^{+0.69}_{-0.00}$	–	$0.00^{+0.15}_{-0.00}$	$0.14^{+0.14}_{-0.14}$	$0.00^{+0.14}_{-0.00}$	$0.00^{+0.48}_{-0.00}$	$0.00^{+0.80}_{-0.00}$
Am. SiO_2	2	$4.9^{+-0.3}_{-1.8}$	–	< 0.1	$6.0^{+0.7}_{-1.9}$	–	$3.8^{+1.2}_{-0.8}$	$0.19^{+5.12}_{-0.19}$	$2.0^{+1.9}_{-1.5}$	$0.77^{+3.82}_{-0.77}$
Am. SiO_2	5	$5.4^{+3.2}_{-+0.2}$	–	$9.1^{+-1.0}_{-9.1}$	$0.00^{+4.33}_{-0.00}$	–	$3.9^{+-0.7}_{-3.9}$	$4.3^{+-1.6}_{-4.3}$	$0.00^{+4.43}_{-0.00}$	$0.00^{+8.01}_{-0.00}$
Ann. SiO_2	0.1	–	$0.12^{+0.82}_{-0.12}$	$0.63^{+1.19}_{-0.63}$	–	$0.12^{+0.43}_{-0.12}$	$0.67^{+-0.13}_{-0.67}$	–	$0.30^{+0.23}_{-0.30}$	$2.2^{+3.0}_{-2.2}$
Ann. SiO_2	2	–	$0.86^{+-0.05}_{-0.86}$	$0.00^{+2.49}_{-0.00}$	$0.58^{+1.49}_{-0.58}$	$0.79^{+-0.26}_{-0.79}$	$0.36^{+1.15}_{-0.36}$	$7.6^{+0.3}_{-5.5}$	$3.2^{+-0.7}_{-3.2}$	$7.6^{+0.6}_{-6.5}$

Dust species	Grain size	Sz 50	PDS 70	GW Lup	IM Lup	Sz 98	V1094 Sco	RNO 90	WA Oph 6
χ^2_r		4.9	64.7	6.9	1.7	8.5	6.0	1.6	8.3
Am. Mg_2SiO_4	0.1	–	–	–	$0.00^{+2.48}_{-0.00}$	$0.00^{+9.40}_{-0.00}$	–	$3.9^{+18.1}_{-3.9}$	–
Am. Mg_2SiO_4	2	< 0.1	$33.4^{+2.8}_{-8.4}$	$0.00^{+10.02}_{-0.00}$	$1.7^{+27.1}_{-1.7}$	$32.6^{+25.5}_{-14.0}$	–	$17.7^{+36.9}_{-17.7}$	$0.00^{+3.20}_{-0.00}$
Am. Mg_2SiO_4	5	$72.8^{+13.1}_{-31.4}$	$0.63^{+6.30}_{-0.63}$	$61.1^{+9.2}_{-33.3}$	$73.4^{+2.2}_{-73.4}$	$42.8^{+9.2}_{-42.6}$	$11.0^{+41.3}_{-11.0}$	$52.0^{+12.8}_{-52.0}$	$33.9^{+44.7}_{-18.0}$
Forsterite	0.1	$0.90^{+-0.23}_{-0.90}$	$6.0^{+0.2}_{-0.3}$	$1.1^{+0.6}_{-+0.1}$	$1.6^{+0.7}_{-0.8}$	$0.56^{+0.47}_{-0.09}$	$2.6^{+0.6}_{-1.7}$	$0.39^{+0.93}_{-0.24}$	$3.3^{+0.7}_{-1.5}$
Forsterite	2	$0.38^{+3.53}_{-0.38}$	$5.6^{+2.5}_{-1.0}$	$5.6^{+3.8}_{-4.8}$	$0.60^{+9.17}_{-0.60}$	$3.7^{+5.0}_{-2.6}$	$6.2^{+4.0}_{-5.2}$	$4.0^{+5.9}_{-4.0}$	$3.4^{+4.4}_{-3.4}$
Am. $MgSiO_3$	0.1	$0.49^{+0.54}_{-0.49}$	$31.0^{+1.4}_{-1.4}$	$2.3^{+5.0}_{-0.3}$	$6.7^{+6.7}_{-3.1}$	$15.4^{+5.6}_{-4.6}$	$0.00^{+0.55}_{-0.00}$	$5.9^{+4.3}_{-4.1}$	$0.09^{+1.82}_{-0.09}$
Am. $MgSiO_3$	2	$0.00^{+0.63}_{-0.00}$	$13.6^{+3.3}_{-2.9}$	$14.1^{+0.9}_{-14.1}$	$11.2^{+9.9}_{-11.2}$	$4.3^{+1.4}_{-4.3}$	–	$12.4^{+0.9}_{-12.4}$	$0.48^{+7.22}_{-0.48}$
Am. $MgSiO_3$	5	$21.7^{+29.1}_{-16.9}$	$0.00^{+3.16}_{-0.00}$	$8.1^{+27.5}_{-8.1}$	$0.00^{+32.63}_{-0.00}$	$0.00^{+8.14}_{-0.00}$	$46.6^{+18.6}_{-32.2}$	$0.00^{+23.34}_{-0.00}$	$47.6^{+1.5}_{-47.6}$
Enstatite	0.1	$0.57^{+0.09}_{-0.57}$	$1.0^{+0.1}_{-0.3}$	$0.46^{+0.42}_{-0.17}$	$1.1^{+0.7}_{-0.5}$	$0.00^{+0.32}_{-0.00}$	$2.3^{+0.3}_{-1.8}$	$0.06^{+0.63}_{-0.06}$	$2.4^{+0.3}_{-1.1}$
Enstatite	2	$0.90^{+0.78}_{-0.90}$	$4.5^{+0.9}_{-0.3}$	$2.2^{+2.1}_{-1.6}$	$1.9^{+4.9}_{-1.5}$	$0.56^{+1.44}_{-0.56}$	$8.2^{+-2.2}_{-7.8}$	$1.7^{+2.9}_{-1.7}$	$4.7^{+1.7}_{-4.0}$
Am. SiO_2	0.1	$0.00^{+0.21}_{-0.00}$	$0.34^{+0.03}_{-0.34}$	–	$0.00^{+0.73}_{-0.00}$	$0.05^{+0.24}_{-0.05}$	$0.25^{+1.86}_{-+0.01}$	$0.00^{+0.23}_{-0.00}$	$0.01^{+0.95}_{-0.01}$
Am. SiO_2	2	–	$0.00^{+0.71}_{-0.00}$	–	–	–	$0.00^{+0.31}_{-0.00}$	–	–
Am. SiO_2	5	$0.00^{+1.89}_{-0.00}$	$3.8^{+-0.7}_{-3.8}$	–	–	$0.00^{+1.32}_{-0.00}$	$16.8^{+8.3}_{-12.3}$	$0.93^{+3.92}_{-0.93}$	$0.00^{+1.08}_{-0.00}$
Ann. SiO_2	0.1	$2.4^{+-0.2}_{-2.0}$	–	$1.3^{+1.5}_{-0.5}$	$1.6^{+0.3}_{-1.6}$	< 0.1	$5.9^{+-2.1}_{-5.0}$	< 0.1	$1.7^{+1.6}_{-0.9}$
Ann. SiO_2	2	–	$0.00^{+0.21}_{-0.00}$	$3.7^{+0.5}_{-3.1}$	$0.12^{+0.88}_{-0.12}$	$0.00^{+0.15}_{-0.00}$	$0.00^{+2.99}_{-0.00}$	$0.92^{+0.10}_{-0.92}$	$2.5^{+0.2}_{-2.5}$

Appendix D: Best-fit disk parameters.

Table D.1. Disk parameters from our fit with the DHS_nat set of opacities.

	$r_{\rm in}$ (au)	$T_{\rm surface,in}$ (K)	$q_{\rm surface}$	$T_{\rm midplane,in}$ (K)	$q_{\rm midplane}$	$w_{\rm rim}$ (au)	$T_{\rm rim}$ (K)
CX Tau	$0.92^{+0.06}_{-0.45}$	1700^{+-28}_{-421}	$-0.69^{+0.08}_{-0.37}$	212^{+22}_{-+2}	$-1.91^{+0.98}_{-0.35}$	$0.0004^{+0.0002}_{-0.0002}$	806^{+385}_{-+18}
CY Tau	$0.09^{+0.16}_{-0.06}$	1022^{+460}_{-453}	$-2.79^{+2.19}_{-+0.53}$	371^{+209}_{-90}	$-0.85^{+0.06}_{-1.57}$	$0.0064^{+0.0010}_{-0.0044}$	1079^{+455}_{-94}
BP Tau	$0.17^{+0.71}_{-+0.04}$	1084^{+-28}_{-586}	$-0.28^{+-0.32}_{-2.20}$	343^{+-20}_{-98}	$-0.57^{+-0.03}_{-1.04}$	$0.0025^{+0.0000}_{-0.0017}$	1319^{+219}_{-405}
FT Tau	$0.07^{+0.72}_{-+0.03}$	730^{+859}_{-+211}	$-2.68^{+1.74}_{-+0.12}$	468^{+-52}_{-217}	$-0.55^{+-0.04}_{-1.26}$	$0.0051^{+-0.0010}_{-0.0046}$	1243^{+208}_{-287}
DF Tau	$0.08^{+0.29}_{-0.02}$	1092^{+243}_{-526}	$-0.19^{+-0.35}_{-1.05}$	562^{+596}_{-242}	$-0.54^{+-0.07}_{-1.99}$	$0.0582^{+0.0162}_{-0.0480}$	1167^{+276}_{-280}
DL Tau	$0.06^{+0.03}_{-0.02}$	1139^{+361}_{-580}	$-0.95^{+0.44}_{-1.56}$	859^{+239}_{-197}	$-0.60^{+0.03}_{-0.05}$	$0.0158^{+0.0249}_{-0.0065}$	1401^{+168}_{-530}
DM Tau	$0.11^{+-0.05}_{-0.08}$	472^{+169}_{-+62}	$-0.26^{+0.02}_{-0.02}$	246^{+102}_{-+34}	$-0.39^{+0.03}_{-+0.01}$	$0.0001^{+0.0008}_{-+0.0001}$	1712^{+-68}_{-717}
AA Tau	$0.51^{+0.40}_{-0.16}$	539^{+549}_{-+23}	$-2.96^{+2.24}_{-+1.03}$	314^{+53}_{-28}	$-1.02^{+0.11}_{-0.91}$	$0.0055^{+-0.0002}_{-0.0036}$	963^{+301}_{-37}
DN Tau	$0.30^{+0.59}_{-0.23}$	1162^{+137}_{-579}	$-0.26^{+-0.02}_{-1.59}$	284^{+193}_{-46}	$-0.75^{+0.20}_{-1.15}$	$0.0025^{+0.0024}_{-0.0014}$	987^{+378}_{-106}
LkCa 15	$0.40^{+0.38}_{-+0.11}$	447^{+170}_{-6}	$-0.09^{+-0.01}_{-0.13}$	175^{+-8}_{-20}	$-0.42^{+-0.02}_{-0.12}$	$0.0004^{+-0.0000}_{-0.0002}$	1760^{+-9}_{-237}
DR Tau	$0.16^{+0.27}_{-0.10}$	1354^{+-417}_{-898}	$-0.37^{+-0.15}_{-1.22}$	513^{+422}_{-150}	$-0.50^{+-0.01}_{-0.10}$	$0.0630^{+-0.0023}_{-0.0427}$	1018^{+536}_{-135}
RW Aur A	$0.96^{+-0.13}_{-0.89}$	1495^{+-60}_{-961}	$-2.05^{+1.23}_{-0.61}$	241^{+307}_{-3}	$-0.80^{+0.34}_{-+0.06}$	$0.0050^{+0.0484}_{-+0.0009}$	1149^{+356}_{-192}
RW Aur B	$0.27^{+0.44}_{-0.21}$	591^{+847}_{-101}	$-0.57^{+0.21}_{-0.06}$	220^{+58}_{-25}	$-0.56^{+0.21}_{-0.77}$	$0.0009^{+0.0043}_{-0.0006}$	1758^{+-14}_{-245}
SY Cha	$0.16^{+0.42}_{-0.01}$	425^{+365}_{-+11}	$-1.86^{+1.24}_{-0.13}$	335^{+22}_{-90}	$-0.56^{+-0.03}_{-0.62}$	$0.0057^{+-0.0008}_{-0.0043}$	1216^{+245}_{-163}
TW Hya	$0.40^{+-0.02}_{-0.25}$	447^{+340}_{-+47}	$-0.16^{+-0.03}_{-0.16}$	201^{+49}_{-1}	$-0.53^{+0.11}_{-+0.01}$	$0.0001^{+0.0002}_{-+0.0000}$	1755^{+-102}_{-570}
VW Cha A	$0.82^{+0.00}_{-0.57}$	763^{+158}_{-165}	$-1.57^{+0.70}_{-0.46}$	274^{+101}_{-10}	$-0.75^{+0.20}_{-0.05}$	$0.0027^{+0.0092}_{-+0.0001}$	1758^{+8}_{-308}
WX Cha A	$0.08^{+0.61}_{-0.05}$	1144^{+192}_{-433}	$-0.16^{+-0.62}_{-1.91}$	422^{+312}_{-177}	$-0.51^{+0.00}_{-1.67}$	$0.0172^{+0.0149}_{-0.0134}$	1285^{+178}_{-216}
XX Cha	$0.21^{+0.74}_{-+0.00}$	568^{+237}_{-79}	$-1.51^{+0.67}_{-0.87}$	305^{+2}_{-83}	$-0.61^{+-0.03}_{-1.17}$	$0.0041^{+0.0003}_{-0.0033}$	1079^{+202}_{-192}
Sz 50	$0.02^{+0.18}_{-0.01}$	445^{+619}_{-+34}	$-2.39^{+1.92}_{-0.22}$	560^{+899}_{-282}	$-0.42^{+-0.03}_{-0.26}$	$0.0222^{+-0.0036}_{-0.0191}$	967^{+135}_{-136}
PDS 70	$0.52^{+0.10}_{-0.24}$	773^{+94}_{-8}	$-2.89^{+1.08}_{-+0.05}$	195^{+17}_{-4}	$-1.49^{+0.62}_{-0.46}$	$0.0002^{+0.0002}_{-0.0000}$	1793^{+-16}_{-187}
GW Lup	$0.58^{+0.12}_{-0.28}$	1261^{+247}_{-456}	$-0.22^{+-0.46}_{-2.31}$	272^{+36}_{-8}	$-1.49^{+0.57}_{-0.37}$	$0.0005^{+0.0006}_{-0.0002}$	1061^{+280}_{-184}
IM Lup	$0.30^{+0.59}_{-0.01}$	1274^{+43}_{-553}	$-0.40^{+-0.02}_{-0.59}$	287^{+18}_{-56}	$-0.60^{+-0.03}_{-0.59}$	$0.0027^{+0.0006}_{-0.0019}$	1424^{+165}_{-335}
Sz 98	$0.51^{+0.37}_{-0.12}$	524^{+611}_{-+117}	$-0.03^{+-0.10}_{-2.38}$	342^{+50}_{-29}	$-0.98^{+0.07}_{-0.64}$	$0.0054^{+0.0004}_{-0.0036}$	1033^{+505}_{-131}
V1094 Sco	$0.03^{+0.65}_{-0.01}$	1232^{+118}_{-558}	$-1.87^{+0.25}_{-0.95}$	514^{+24}_{-305}	$-0.51^{+0.02}_{-2.08}$	$0.0098^{+0.0053}_{-0.0091}$	1171^{+-61}_{-308}
RNO 90	$0.61^{+0.29}_{-0.15}$	765^{+285}_{-278}	$-0.23^{+-0.29}_{-2.23}$	294^{+29}_{-24}	$-0.67^{+0.05}_{-0.23}$	$0.0056^{+0.0040}_{-0.0017}$	1510^{+130}_{-304}
WA Oph 6	$0.64^{+0.14}_{-0.51}$	540^{+600}_{-32}	$-3.00^{+2.41}_{-+0.22}$	254^{+233}_{-3}	$-0.79^{+0.22}_{-0.17}$	$0.0084^{+0.0069}_{-0.0036}$	823^{+440}_{-+25}

Appendix E: Fit to PDS 70 with GRF opacities.

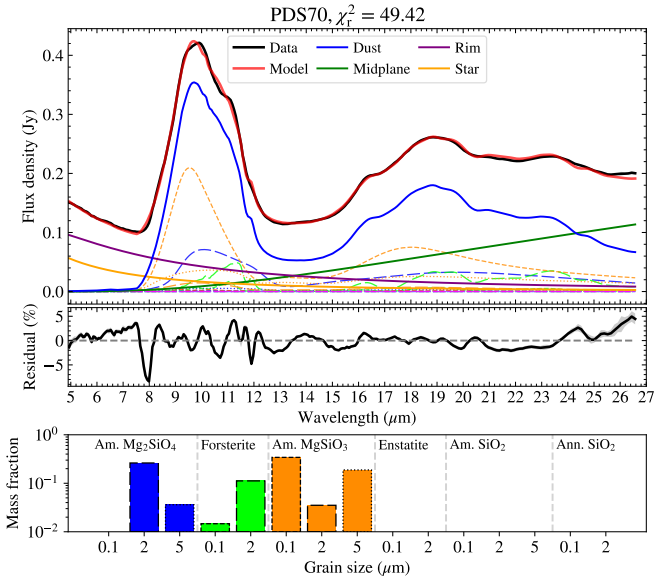

Fig. E.1. Fits to the spectrum of PDS 70 with GRS opacities (including annealed silica), using the [0.1, 2, 5 am.] grain size set.

Appendix F: Fit residuals

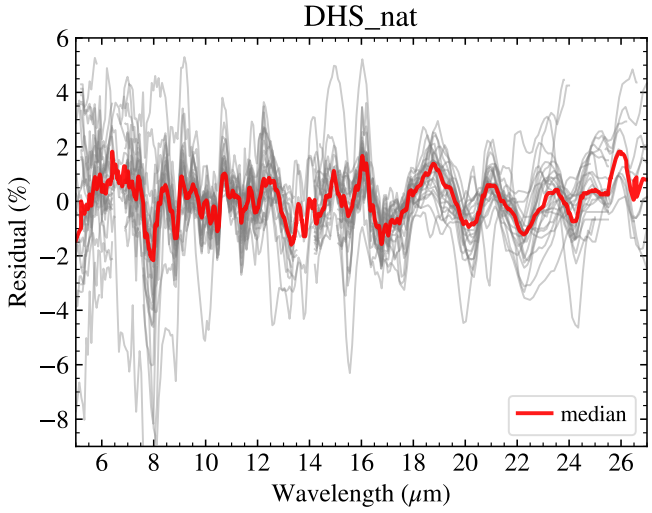

Fig. F.1. Fit residuals (gray lines) plotted on top of each other with the grain size set [0.1, 2, 5 am.], with annealed silica. The red line shows the median of the residuals.

Appendix G: Simulating Spitzer/IRS low-resolution spectroscopy

To simulate a Spitzer/IRS observation, we degraded the MIRI spectrum of XX Cha to the resolving power and S/N of Spitzer/IRS low-resolution spectroscopy. We produced two versions of the degraded spectrum: one based on the original MIRI spectrum, which includes all molecular line emission, and another based on the line-removed spectrum that was also used for our MIRI dust compositional fits. We then applied our spectral decomposition routine to the degraded spectra, and the resulting best fits are shown in Fig. G.1. In general, the derived dust mass fractions are broadly consistent between the two cases, although the effects of the degeneracy between large amorphous Mg-silicate grains are noticeable in the mass fractions. In addition, the constraints on annealed silica are relatively weak, as its characteristic features at 12.6 and 16.1 μm become rather noisy. Consequently, the fit cannot efficiently distinguish between amorphous and annealed silica. Across our sample, the impact of molecular lines on the dust features is minor outside a few narrow wavelength regions known to be strongly affected by molecular emission (e.g., around 6.5 μm and 14.5 μm). The differences between the original MIRI spectra degraded to the resolving power of Spitzer and the line-removed versions are typically only 0.5–1%. This finding is expected to remain valid for other T Tauri and Herbig objects with relatively strong silicate features, but is expected to break down for VLMSs, which tend to exhibit weaker silicate features and stronger molecular line emission (Jang et al. 2025).

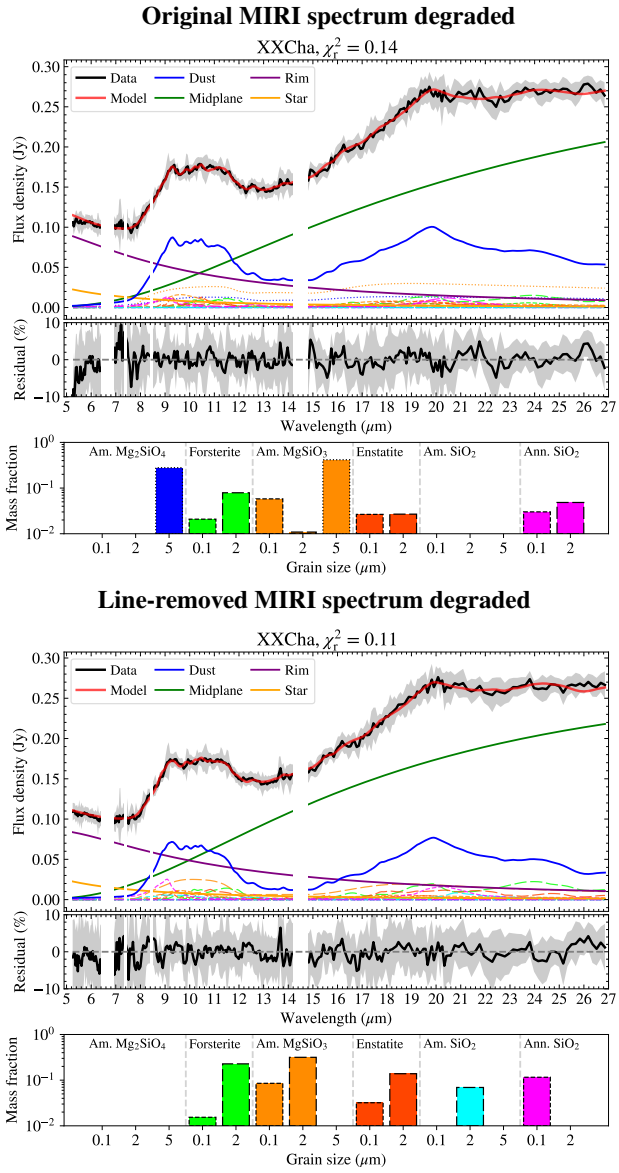

Fig. G.1. Fits to the MIRI spectra of XX Cha degraded to the resolving power and S/N of Spitzer/IRS low-resolution spectroscopy. The upper panel shows the result obtained using the original MIRI spectrum of XX Cha as input, which includes all molecular line emission. The lower panel shows the same analysis performed on the line-removed MIRI spectrum.